Control Engineering Practice 127 (2022) 105282

Contents lists available at ScienceDirect

Control Engineering Practice

journal homepage: www.elsevier.com/locate/conengprac

Robust adaptive backstepping DP control of ROVs

Sveinung Johan Ohrem [a,*], Herman Biørn Amundsen [a,b], Walter Caharija [a,d], Christian Holden [c]

[a] Aquaculture Operations and Robotics, SINTEF Ocean AS, Trondheim, Norway
[b] Department of Engineering Cybernetics, Norwegian University of Science and Technology, Trondheim, Norway
[c] Department of Mechanical and Industrial Engineering, Norwegian University of Science and Technology, Trondheim, Norway
[d] Offshore Marine Center, Siemens Energy AS, Trondheim, Norway

ARTICLE INFO

Keywords:
Adaptive control
Remotely operated vehicle
Aquaculture
Dynamic positioning
Matrosov's theorem

ABSTRACT

Dynamic positioning is an important control feature for an underwater remotely operated vehicle. This paper presents a nonlinear dynamic positioning controller suited for application to vehicles with model uncertainties, operating in environments with unpredictable disturbances, such as an aquaculture net cage. The proposed controller combines the backstepping approach with an adaptation term to ensure robustness. Using Lyapunov theory and Matrosov's theorem the origin of the closed-loop system is proven to be: (i) globally asymptotically stable when assuming persistency of excitation, and (ii) stable and bounded, with the true position converging to the desired position if there is no persistency of excitation. This paper also presents results from simulations where the proposed controller is contextualized and compared to similar controllers, showing promising results. Finally, as the main result of the manuscript that demonstrates the effectiveness of the proposed control law, an extensive field trial campaign is conducted at a full-scale aquaculture site using an industrial ROV where the proposed controller is successfully tested under realistic operational conditions.

1. Introduction

1.1. Background

In recent years, the use of remotely operated vehicles (ROVs) has sharply increased. ROVs are used in areas such as oil and gas, marine biology, marine archaeology, aquaculture, and many more. The main drivers behind this increased adaption of ROVs are cost reductions as well as the increased availability of navigation aid sensors such as Doppler velocity logs (DVLs) and ultra short base line (USBL) systems.

Many subsea ROV operations require the vehicle to keep a constant position and a constant orientation, e.g., to perform station keeping. When station keeping is performed manually the operator steers the ROV based on visual inputs (i.e., cameras), visual landmarks, depth measurements and compass bearing. Furthermore, while manually keeping the ROV in position the operator must often simultaneously execute a visual inspection of, e.g., a subsea structure, or a subsea intervention operation. The operators are therefore given multiple concurring and demanding tasks that bear high responsibility: precise vehicle steering combined with thorough visual inspections and/or interventions. Moreover, such tasks must be executed in a short time and in varying sea states. A dynamic positioning (DP) system is therefore of much help to an ROV operator since it ensures that the ROV holds the desired position, and automatically compensates for the disturbances arising from e.g. ocean currents, hence avoiding drift.

1.2. Motivation

The sea-based aquaculture sector is also witnessing significant growth in ROV usage for inspection and intervention tasks inside and outside fish cages. Subsea inspection of aquaculture net pens is fundamental to assess the integrity of the net, i.e., to estimate wear, tear, and biofouling, as well as to locate net holes. Net holes are among the primary causes of farmed fish escapes (Thorvaldsen et al., 2015) resulting in loss of production and unwanted interference of the bred species on the wild fish. In 2010 it was reported that more than two thirds of the registered fish escape incidents from fish farms in Norway were related to holes in the net (Jensen et al., 2010). ROVs are also used for intervention tasks such as net cleaning. Net cleaning is conducted every 2–4 weeks in order to reduce or prevent the growth of harmful organisms on the nets (Bannister et al., 2019). In aquaculture operations the ROV position must be precisely controlled, as a collision with the net cage may cause holes and make fish escape. The level of autonomy of ROV operations in aquaculture must therefore be increased to: (1) reduce the fatigue on ROV operators; (2) increase the precision, speed and the quality of inspections; and (3) extend the weather operational window.

Technologies such as USBL systems and DVLs can measure position and velocity underwater, respectively, and can therefore provide the operator with estimates of the ROV position with respect to the support vessel, and the ROV velocity. Furthermore, such systems enable the

* Corresponding author.
E-mail address: sveinung.ohrem@sintef.no (S.J. Ohrem).

https://doi.org/10.1016/j.conengprac.2022.105282
Received 30 June 2021; Received in revised form 20 July 2022; Accepted 21 July 2022
Available online xxxx

use of more advanced underwater control and navigation methods in the aquaculture domain as exemplified in Rundtop and Frank (2016), where a DVL is mounted on an ROV, but rather than pointing downwards, it is pointing forwards. Thus it can be used to lock on the net structure. Furthermore, in Rundtop and Frank (2016), a USBL is shown to be able to transmit position data through a net pen consisting of hundreds of thousands of fish. According to Rundtop and Frank (2016), it is possible to accurately estimate the position of the ROV with respect to the net pen and hence, develop closed-loop control systems for autonomous navigation inside a fish cage that relieve the ROV operator from continuous steering. An autonomous net-following algorithm utilizing a forward facing DVL measurements is demonstrated in Amundsen et al. (2022).

A closed-loop control system that makes an ROV operate autonomously in a sensitive and challenging environment, such as an aquaculture net pen, must show robustness to environmental disturbances and model uncertainties. An underwater vehicle such as an ROV is exposed to forces arising from tether drag, ocean currents and waves, and its mathematical model suffers from uncertainties, especially in its hydrodynamic parameters. The model may also vary in time if, for instance, the payload is changed from one mission to another, or if the ROV picks up an object or interacts with the structure with its manipulator. A DP control algorithm must therefore ensure that the desired tasks are performed within the requirements and with a minimal deviation from the desired position or path, even when the vehicle is affected by disturbances and when its model parameters are highly uncertain or even unknown.

1.3. Previous work and state-of-the-art

Rendering ROV operations more autonomous is an active area of research due to the growth experienced by the whole blue economy. In particular, control systems allowing for autonomous path following and navigation of vehicles such as ROVs are proposed in Bibuli et al. (2012), Caharija et al. (2016) and Vasilijević et al. (2017), while Capocci et al. (2018) and Omerdic and Roberts (2004) address thruster fault tolerance of ROVs involved in DP operations. Furthermore, state estimation solutions for DP and other tasks of ROVs are given in Candeloro et al. (2012), Kinsey and Whitcomb (2007) and Zhao et al. (2012). Robustness of ROV control solutions, such as DP control, is therefore a key performance factor in subsea operations.

1.3.1. Feedback linearizing control

Non-linear control algorithms have received increased focus due to the non-linear behavior of marine craft, and feedback linearizing controllers are often able to cancel or exploit the non-linear effects if the parameters of the system are known (Fossen & Pettersen, 2014; Holden & Pettersen, 2007; Moe et al., 2014). Having been applied to marine vehicles since its advent in the 1990's, feedback linearizing control is a well-proven control methodology which is still applied for DP control (Fernandes et al., 2015; Landstad et al., 2021). In both Fernandes et al. (2015) and Landstad et al. (2021), feedback linearizing controllers are successfully demonstrated in field trials. The drawback of the feedback linearizing controller is the requirement of exact parameter knowledge, which for an ROV or any underwater vehicle is difficult to obtain and may change with varying sea-states (Sørensen, 2013).

1.3.2. Adaptive and backstepping control

Adaptive control algorithms can alleviate the requirement of exact parameter knowledge introduced by feedback linearizing controllers. Adaptation can be introduced to the control scheme in several different manners and the adaptation is often augmenting a different control scheme, e.g., PD controllers, feedback linearizing controllers, backstepping controllers, or sliding mode controllers.

The work presented in Smallwood and Whitcomb (2004) compares linear, non-linear and adaptive control algorithms in both simulations and field trials for a trajectory tracking problem. One of the presented adaptive controllers, a PD controller with parameter adaptation, ensures convergence of the velocity errors, and a cross-term must be introduced in the adaptation law to ensure convergence of the position error.

In Antonelli et al. (2003), a PD controller with adaptation is presented. It is argued that a regressor matrix encompassing all unknown parameters of an underwater vehicle, e.g., mass matrix parameters, damping terms, etc., is very complex and not practical to implement and hence, only the external hydrodynamic effects, i.e., the restoring forces and the ocean currents, are adapted and compensated. A PD controller with adaptation for an ROV, with experimental results, is presented in Hoang and Kreuzer (2007), but adaptation of the ROVs parameters is not included.

A vectorial backstepping approach, in combination with a nonlinear passive observer, is applied to an offshore vessel in Fossen and Grovlen (1998) and the proposed feedback controller relies on knowledge of the parameters of the mass and damping matrices. An *adaptive* backstepping approach is utilized in Zhu and Gu (2011), and the parameters of a work class ROV, i.e., the mass, damping and Coriolis terms, are included in the adaptation, while the ocean currents are compensated by a sliding term and thus not covered by the adaptive term. In Du et al. (2018), an adaptive backstepping DP control law is designed for surface vessels, but neither the nonlinear damping terms nor the ocean current velocity are estimated. As such, none of the works Antonelli et al. (2003), Du et al. (2018), Fossen and Grovlen (1998), Fossen and Sagatun (1991), Hoang and Kreuzer (2007) and Zhu and Gu (2011) adapt both the unknown system parameters and the external disturbance forces.

In Antonelli et al. (2001), a controller similar to the one presented in Antonelli et al. (2003) is successfully demonstrated in a field trial. Experimental results of a model reference adaptive controller (MRAC) is demonstrated in Makavita et al. (2017). The MRAC, however, does not adapt the parameters of the underlying model of the system, but rather adapts the controller parameters to ensure that the output of the system tracks the output of a reference model (Ioannou & Sun, 2012, Ch. 6).

When applying the backstepping control scheme, an alternative to adaptive control is integral action. In particular, Skjetne and Fossen (2004) gives an analysis of different techniques that combine backstepping with integral action, arguing that pure integral action is sensitive to the chosen control gain and that the behavior may change drastically if control design is not performed with great care. It is furthermore argued that adaptive control may have advantages when doing trajectory tracking.

The state-of-the-art in adaptive backstepping control appears to include adaptation of either the unknown system parameters *or* the unknown disturbances, not both. Further, most studies on adaptive backstepping control seems to not include results from experimental trials.

1.3.3. Sliding mode control

Passivity-based adaptive controllers utilizing theory from sliding mode control are presented in Fossen and Sagatun (1991) to overcome the input uncertainties often present in underwater vehicles due to non-linearity in the thruster characteristics.

A sliding mode DP control law for underwater vehicles that predicts unknown hydrodynamic effects using a Gaussian process regressor is presented in Lima et al. (2020). The control law does not estimate the underlying parametric uncertainties and is not demonstrated in field trials.

Adaptive sliding mode controllers appear in several recent scientific works, and variations of adaptive sliding mode seems to be the state-of-the-art in marine vehicle control.

In Wang et al. (2021) sliding mode is combined with adaptive disturbance estimation, and simulation results show an improvement in the ROV's maneuvering capabilities when the adaptation is introduced.

In Yan et al. (2019) an underactuated autonomous underwater vehicle (AUV) is controlled using an adaptive sliding mode controller that utilizes a neural network to estimate the AUV's parameters. The external disturbance is compensated by utilizing an auxiliary control vector which acts as an estimate of the disturbance. Simulation results show that the method works very well, but no experimental results exist.

In Qiao and Zhang (2019), two novel adaptive sliding mode controllers are proposed. The controllers consist of two loops, i.e., a kinematic controller and a dynamic controller. The external disturbance and the upper bound of the system uncertainty are estimated through adaptation and then used as controller parameters. Comparative simulation results show fast convergence rate and strong robustness, but no field experiments are presented.

The interested reader is referred to, e.g., Karimi and Lu (2021) for further reading on guidance and control methodologies for marine vehicles.

1.4. Contributions

Based on the existing literature, adaptive sliding mode control appears to be the state-of-the-art in marine vehicle control. However, based on the reviewed literature and the reported field trials therein, a control law that combines backstepping with adaptation to handle uncertainties seems promising in applications where precise control as well as robustness towards uncertainties and disturbances are required. Furthermore, no adaptive backstepping controller that adapts both the unknown system parameters and the unknown disturbances could be found in literature. Nor could experimental validations of adaptive backstepping controllers.

Hence, a new solution had to be synthesized, inspired by Antonelli et al. (2003), Fossen and Grovlen (1998), Fossen and Sagatun (1991), Hoang and Kreuzer (2007) and Zhu and Gu (2011). The contributions of this paper are therefore twofold and encompass (1) the control law, which combines adaptation of both the external disturbance forces and the model parameters, and (2) the experimental validation of the adaptive backstepping DP controller in a full-scale field trial. Validations of adaptive backstepping controllers in field-trials appears to be lacking in the available literature. The latter is thus to be regarded as the main contribution of this manuscript.

1.4.1. First contribution: The control law

A robust adaptive backstepping DP control law which adapts both the unknown ocean current and the unknown mass and damping parameters of the ROV is proposed. The proposed control structure extends the work of Antonelli et al. (2003), Fossen and Grovlen (1998), Fossen and Sagatun (1991), Hoang and Kreuzer (2007) and Zhu and Gu (2011) by combining backstepping with adaptation. The proposed controller does not require any knowledge of the ROVs mass and damping parameters.

The origin of the closed-loop error system is shown to be stable and bounded by Lyapunov analysis. The position error is furthermore proven to converge to zero. Using Matrosov's Theorem, it is also shown that the uncertain parameters will converge when a persistently exciting (PE) signal is applied, rendering the origin of the error system globally asymptotically stable in this case.

1.4.2. Second contribution: The experimental validation

The proposed control law is applied to an Observation-class ROV, and the station-keeping capabilities of the controller are verified via simulations using the FhSim framework (Reite et al., 2014; Su et al., 2019). The proposed controller is compared, in simulations, to an adaptive backstepping controller that only adapts the external disturbance, and to a backstepping controller with integral augmentation.

Results from full-scale experiments are presented to validate and illustrate the theoretical results. The experimental results show that the controller successfully maintains the ROV's position with the chosen heading, in spite of the derivation of the controller being based on several simplifying assumptions. The trials were conducted at a full-scale aquaculture site under realistic operational conditions. To the authors' knowledge, no analogous experimental results demonstrating the use of adaptive backstepping DP controllers for ROVs in an industrial context exist in literature. This is the main contribution of the presented work.

1.5. Paper outline

The paper is divided into the following sections: Section 2 presents the control plant model of an Observation-class ROV. This is used to develop the control law. In Section 3, the control algorithm is derived by applying Lyapunov stability theory and Matrosov's Theorem. Section 4 contains simulation and experimental results and Section 5 concludes the paper.

2. Control plant model

The dynamic behavior of an ROV can be expressed using two reference frames, the North-East-Down (NED) frame and the body-fixed BODY frame. As in Fernandes et al. (2015), a control plant model solely concerning the controlled degrees of freedom is proposed in this paper. The following assumptions are used in the development of the control plant model and are only applied to simplify the controller development.

Assumption 1. The ROV is symmetric about the port-starboard, fore–aft and bottom–top axes.

Assumption 2. The roll and pitch angles are passively stabilized by gravity and are assumed small ($\phi, \theta \approx 0$). These are therefore not included in the model.

Assumption 3. The vehicle's center of gravity (CG) and the center of buoyancy (CB) are located along the same vertical axis in the BODY frame. The center of origin (CO) of the BODY-fixed frame and CG are coinciding.

Remark 1. Assumptions 1–3 are common assumptions when modeling ROVs (Antonelli, 2014).

Remark 2. Assumptions 1 and 3 imply that the gravitational forces are only present in the vertical z-direction, i.e., $\boldsymbol{g}(\boldsymbol{\eta}) = \begin{bmatrix} 0 & 0 & g_z & 0 \end{bmatrix}^{\mathrm{T}}$.

Assumption 4. The contributions from the Coriolis and centripetal forces are dominated by the linear and nonlinear damping terms and are therefore not taken into account.

Remark 3. The vehicle operates at relatively low speeds. As such, the contribution from the Coriolis and centripetal terms will be small and hence, for control plant modeling purposes, the Coriolis and centripetal effects are not considered.

Assumption 5. The effects of ocean current disturbances as well as wave-induced forces are assumed to be constant and irrotational forces in the NED frame and their effects are projected onto the vehicle. These forces are only considered present in the horizontal plane, i.e., $\boldsymbol{\tau}_c = \begin{bmatrix} \tau_N & \tau_E & 0 & 0 \end{bmatrix}^{\mathrm{T}}$.

Remark 4. Modeling the ocean current and wave induced forces as a force disturbance is a simplified approach which is useful when designing DP control systems as it obviates the need for e.g., the relative velocity vector which may require measurements of the ocean current

velocity (Antonelli et al., 2003); (Antonelli, 2014, Ch. 2.4.3). The ocean current flow pattern inside a fish cage is complex, but the flow speed is reduced compared to outside the cage (Jónsdóttir et al., 2021). As such, Assumption 5 may seem somewhat strict. However, it is only used when deriving the control law, and it will be shown through experiments that the controller is capable of suppressing the ocean current disturbance.

Further, Fossen (2011, Ch. 8.2) suggests that induced wave forces can be separated into two different effects: a wave-frequency motion that is observed as a zero-mean oscillatory effect and a wave drift force that is observed as a non-zero, slowly varying component. While a control system should compensate for the wave drift forces, the zero-mean wave-frequency motions should instead be removed using wave filtering (Fossen, 2011). As such, wave-frequency motions are not included in the control plant model.

Assumption 6. The parameters of the mass and damping matrices, as well as the gravitational force, are constant.

Remark 5. Assumption 6 is introduced to simplify the derivation of the adaptation law. Constant parameter assumptions are common in adaptive control (Ioannou & Sun, 2012); (Fossen, 2011, Ch. 13.2.5).

The dynamics of the vehicle in four degrees of freedom is expressed with the following control plant model, often called a DP model (Fossen, 2011)

$$\dot{\boldsymbol{\eta}} = \boldsymbol{J}(\boldsymbol{\eta})\boldsymbol{\nu} \tag{1}$$

$$\boldsymbol{M}\dot{\boldsymbol{\nu}} + \boldsymbol{D}_l\boldsymbol{\nu} + \boldsymbol{D}_n(\boldsymbol{\nu})\boldsymbol{\nu} + \boldsymbol{g}(\boldsymbol{\eta}) = \boldsymbol{\tau} + \boldsymbol{\tau}_c^b \tag{2}$$

where $\boldsymbol{\eta} = \begin{bmatrix} N & E & D & \psi \end{bmatrix}^{\mathrm{T}}$ is the vector of positions and the attitude expressed in the NED frame, and $\boldsymbol{\nu} = \begin{bmatrix} u & v & w & r \end{bmatrix}^{\mathrm{T}}$ is the vector of linear and angular velocities expressed in the BODY frame, relative to the NED frame. The matrix $\boldsymbol{M} = \boldsymbol{M}_{RB} + \boldsymbol{M}_A > 0, \in \mathbb{R}^{4\times4}$ is the system inertia matrix, which is the sum of the rigid body system inertia matrix $\boldsymbol{M}_{RB} = \boldsymbol{M}_{RB}^{\mathrm{T}} > 0$ and the hydrodynamic added mass inertia matrix $\boldsymbol{M}_A = \boldsymbol{M}_A^{\mathrm{T}} \geq 0$. The matrices $\boldsymbol{D}_l > 0 \in \mathbb{R}^{4\times4}$ and $\boldsymbol{D}_n(\boldsymbol{\nu}) > 0 \in \mathbb{R}^{4\times4}$ represent the linear and nonlinear damping, respectively.

The transformation matrix $\boldsymbol{J}(\boldsymbol{\eta}) \in \mathbb{R}^{4\times4}$ relates the NED and BODY frames

$$\boldsymbol{J}(\boldsymbol{\eta}) = \begin{bmatrix} \boldsymbol{R}(\psi) & \boldsymbol{0}_{3\times1} \\ \boldsymbol{0}_{1\times3} & 1 \end{bmatrix} \tag{3}$$

where the rotation matrix, $\boldsymbol{R}(\psi)$, is

$$\boldsymbol{R}(\psi) = \begin{bmatrix} \cos(\psi) & -\sin(\psi) & 0 \\ \sin(\psi) & \cos(\psi) & 0 \\ 0 & 0 & 1 \end{bmatrix} \tag{4}$$

with $\boldsymbol{R}^{\mathrm{T}}(\psi) = \boldsymbol{R}^{-1}(\psi)$, i.e., $\boldsymbol{J}^{\mathrm{T}}(\boldsymbol{\eta}) = \boldsymbol{J}^{-1}(\boldsymbol{\eta})$.

The vector $\boldsymbol{\tau} \in \mathbb{R}^4$ contains the generalized control forces acting on the different DOFs, while the vector $\boldsymbol{\tau}_c^b \in \mathbb{R}^4$ contains the external disturbance from ocean currents in the BODY frame. The ocean currents inside an aquaculture net cage often have a lower flow speed compared to outside the cages, as such they are assumed constant and irrotational in the NED frame (Assumption 5) and are projected onto the BODY frame as a time-varying force (due to the dependency on $\boldsymbol{J}^{\mathrm{T}}(\boldsymbol{\eta})$) as follows

$$\boldsymbol{\tau}_c^b(t) = \boldsymbol{J}^{\mathrm{T}}(\boldsymbol{\eta})\boldsymbol{\tau}_c = \begin{bmatrix} \tau_N \tau_E & 0 & 0 \end{bmatrix}. \tag{5}$$

Remark 6. Nonlinear damping, represented by the matrix $\boldsymbol{D}_n(\boldsymbol{\nu})$, is often omitted in DP models as the contribution is very small during station keeping. In this work, nonlinear damping is included to increase the robustness of the controller with respect to unmodeled dynamics.

3. Control law

This section introduces a control law based on a vectorial backstepping approach for marine vehicles, first introduced in Fossen and Berge (1997). Further, the proposed controller utilizes a global diffeomorphism to a vessel parallel coordinate system in order to simplify notation throughout the development of the controller. Finally, the proposed controller utilizes adaptation in order to handle uncertainties in the ROV parameters and unknown external disturbances.

3.1. Global diffeomorphism

To simplify the notation and increase readability throughout the development of the controller, a global diffeomorphism is applied as in Holden and Pettersen (2007). A *vessel parallel* coordinate system, which is obtained by rotating the BODY axes an angle ψ about the z axis (akin to Fossen (2011, Ch. 7.5.3)) is used. From (2), (3) and (4) the diffeomorphism $\boldsymbol{\eta}_p \in \mathbb{R}^4$ can be defined as follows

$$\boldsymbol{\eta}_p \triangleq \boldsymbol{J}^{\mathrm{T}}(\psi)\boldsymbol{\eta} = \boldsymbol{J}^{\mathrm{T}}(\psi)\begin{bmatrix} \boldsymbol{p} \\ \psi \end{bmatrix} = \begin{bmatrix} \boldsymbol{R}^{\mathrm{T}}(\psi) & \boldsymbol{0}_{3\times1} \\ \boldsymbol{0}_{1\times3} & 1 \end{bmatrix}\begin{bmatrix} \boldsymbol{p} \\ \psi \end{bmatrix} = \begin{bmatrix} \boldsymbol{p}_p \\ \psi \end{bmatrix} = \boldsymbol{T}(\boldsymbol{\eta}) \tag{6}$$

where $\boldsymbol{p} = \begin{bmatrix} N & E & D \end{bmatrix}^{\mathrm{T}}$. The inverse of $\boldsymbol{T}(\boldsymbol{\eta})$ is

$$\boldsymbol{\eta} = \boldsymbol{J}(\psi)\begin{bmatrix} \boldsymbol{p}_p \\ \psi \end{bmatrix} = \begin{bmatrix} \boldsymbol{R}(\psi) & \boldsymbol{0}_{3\times1} \\ \boldsymbol{0}_{1\times3} & 1 \end{bmatrix}\begin{bmatrix} \boldsymbol{p}_p \\ \psi \end{bmatrix}. \tag{7}$$

Since both $\boldsymbol{T}$ and $\boldsymbol{T}^{-1}$ exists and the derivatives are continuous for all $\boldsymbol{\eta}$ and $\boldsymbol{\eta}_p$, the diffeomorphism is, by the definition in Khalil (2002, Ch. 13.1, p. 508), global.

The time derivative of $\boldsymbol{\eta}_p$ is (function arguments are omitted)

$$\dot{\boldsymbol{\eta}}_p = \begin{bmatrix} \boldsymbol{R}^{-1}\dot{\boldsymbol{p}} + \dot{\boldsymbol{R}}^{-1}\boldsymbol{p} \\ r \end{bmatrix}. \tag{8}$$

Using that $\dot{\boldsymbol{R}}^{-1} = -\boldsymbol{S}(r)\boldsymbol{R}^{-1}$ (Fossen, 2011, Ch. 2.2.1), where $\boldsymbol{S}(r) = -\boldsymbol{S}(r)^{\mathrm{T}}$ is the cross-product operator (Fossen, 2011, Def. 2.2), i.e.,

$$\boldsymbol{S}(r) = \begin{bmatrix} 0 & -r & 0 \\ r & 0 & 0 \\ 0 & 0 & 0 \end{bmatrix}, \tag{9}$$

and $\boldsymbol{p} = \boldsymbol{R}\boldsymbol{p}_p$ results in

$$\begin{aligned} \dot{\boldsymbol{\eta}}_p &= \begin{bmatrix} \boldsymbol{R}^{-1}\dot{\boldsymbol{p}} - \boldsymbol{S}(r)\boldsymbol{R}^{-1}\boldsymbol{R}\boldsymbol{p}_p \\ r \end{bmatrix} \\ &= \begin{bmatrix} \boldsymbol{v} - \boldsymbol{S}(r)\boldsymbol{p}_p \\ r \end{bmatrix} \\ &= \boldsymbol{\nu} - \begin{bmatrix} \boldsymbol{S}(r)\boldsymbol{p}_p \\ 0 \end{bmatrix} \end{aligned} \tag{10}$$

where $\boldsymbol{v} = \begin{bmatrix} u & v & w \end{bmatrix}^{\mathrm{T}}$ is the vector of linear velocities in the BODY frame.

3.2. Proposed control law

Before the control law is presented, some variables are defined for ease of reference: First, consider the position and velocity errors

$$\begin{aligned} \boldsymbol{e}_1(t) &= \boldsymbol{\eta}_p(t) - \boldsymbol{\eta}_{p,d}(t) = \boldsymbol{J}^{\mathrm{T}}(\psi)(\boldsymbol{\eta}(t) - \boldsymbol{\eta}_d(t)) \\ &= \begin{bmatrix} \boldsymbol{R}^{\mathrm{T}}(\boldsymbol{p} - \boldsymbol{p}_d) \\ \psi - \psi_d \end{bmatrix} = \begin{bmatrix} \boldsymbol{R}^{\mathrm{T}}\tilde{\boldsymbol{p}} \\ \tilde{\psi} \end{bmatrix} = \begin{bmatrix} \tilde{\boldsymbol{p}}_p \\ \tilde{\psi} \end{bmatrix} \end{aligned} \tag{11}$$

$$\boldsymbol{e}_2(t) = \boldsymbol{\nu}(t) - \boldsymbol{\nu}_d(t) = \begin{bmatrix} \boldsymbol{v} - \boldsymbol{v}_d \\ r - r_d \end{bmatrix} = \begin{bmatrix} \tilde{\boldsymbol{v}} \\ \tilde{r} \end{bmatrix} \tag{12}$$

where $\boldsymbol{\eta}_p(t) = \boldsymbol{J}^{\mathrm{T}}(\psi)\boldsymbol{\eta}(t)$ is the position and attitude, $\boldsymbol{\eta}(t)$, rotated to the vessel parallel coordinate system; and $\boldsymbol{\eta}_{p,d}(t) = \boldsymbol{J}^{\mathrm{T}}(\psi)\boldsymbol{\eta}_d$ is the desired position and attitude, $\boldsymbol{\eta}_d(t) = \begin{bmatrix} \boldsymbol{p}_d^{\mathrm{T}} & \psi_d \end{bmatrix}^{\mathrm{T}}$, rotated to the vessel parallel coordinate system; with $\boldsymbol{p}_d = \begin{bmatrix} N_d & E_d & D_d \end{bmatrix}^{\mathrm{T}}$. Furthermore, $\boldsymbol{\nu}_d(t) = \begin{bmatrix} \boldsymbol{v}_d^{\mathrm{T}} & r_d \end{bmatrix}^{\mathrm{T}}$ is the desired velocity with $\boldsymbol{v}_d = \begin{bmatrix} u_d & v_d & w_d \end{bmatrix}^{\mathrm{T}}$

in the BODY frame (the function argument t is omitted from now on). The heading angle error is given by $\tilde{\psi}$, whereas $\tilde{\boldsymbol{p}}$ is the position error in the NED frame and $\tilde{\boldsymbol{p}}_p$ is the position error rotated to the vessel parallel coordinate system.

Second, consider a virtual velocity vector, or backstepping variable

$$\boldsymbol{\nu}_v = \boldsymbol{\nu}_d - \boldsymbol{K}_1 \boldsymbol{e}_1 = \begin{bmatrix} u_v & v_v & w_v & r_v \end{bmatrix}^{\mathrm{T}} \tag{13}$$

where $\boldsymbol{K}_1 = \boldsymbol{K}_1^{\mathrm{T}} > 0 \in \mathbb{R}^{4\times4}$ is a matrix of control gains chosen by the user, and another error signal

$$\bar{\boldsymbol{e}}_2 = \boldsymbol{\nu} - \boldsymbol{\nu}_v \,. \tag{14}$$

The control law will now be presented.

Theorem 1. *Given an underwater vehicle described by (1) and (2). If Assumptions 1–6 hold, the control law*

$$\boldsymbol{\tau} = -\boldsymbol{K}_2 \bar{\boldsymbol{e}}_2 - \boldsymbol{e}_1 + \boldsymbol{\Phi}^{\mathrm{T}} \hat{\boldsymbol{\Psi}} \tag{15}$$

where $\boldsymbol{K}_2 = \boldsymbol{K}_2^{\mathrm{T}} > 0 \in \mathbb{R}^{4\times4}$, $\boldsymbol{e}_1$ as in (11), $\bar{\boldsymbol{e}}_2$ as in (14), $\boldsymbol{\Phi} \in \mathbb{R}^{15\times4}$ is a matrix of known signals and $\hat{\boldsymbol{\Psi}} \in \mathbb{R}^{15}$ is an estimate of the unknown system parameters and external disturbances, and the adaptation law

$$\dot{\hat{\boldsymbol{\Psi}}} = -\boldsymbol{\Gamma} \boldsymbol{\Phi} \bar{\boldsymbol{e}}_2 \tag{16}$$

with arbitrary initial conditions $\hat{\boldsymbol{\Psi}}(0) = \hat{\boldsymbol{\Psi}}_0 \in \mathbb{R}^{15}$, where $\boldsymbol{\Gamma} = \boldsymbol{\Gamma}^{\mathrm{T}} > 0 \in \mathbb{R}^{15\times15}$ ensures that the origin of the error system $\boldsymbol{e}_1, \bar{\boldsymbol{e}}_2, \tilde{\boldsymbol{\Psi}} = \hat{\boldsymbol{\Psi}} - \boldsymbol{\Psi}$ is stable, the trajectories of the system bounded, and $\boldsymbol{e}_1, \bar{\boldsymbol{e}}_2$ converge to zero for all initial values.

Proof. The proof is divided into 3 steps.

Step 1: First, consider the time derivative of the position and attitude error from (11):

$$\dot{\boldsymbol{e}}_1 = \dot{\boldsymbol{\eta}}_p - \dot{\boldsymbol{\eta}}_{p,d} = \dot{\boldsymbol{\eta}}_p = \begin{bmatrix} \tilde{\boldsymbol{v}} - \boldsymbol{S}(r)\tilde{\boldsymbol{p}}_p \\ \tilde{r} \end{bmatrix} \tag{17}$$

using (10) and $\tilde{\boldsymbol{v}} = \dot{\tilde{\boldsymbol{p}}}_p$. Now consider a Lyapunov function candidate

$$V_1(\boldsymbol{e}_1) = \frac{1}{2} \boldsymbol{e}_1^{\mathrm{T}} \boldsymbol{e}_1 \geq 0 \;\; \forall \;\; \boldsymbol{e}_1. \tag{18}$$

The derivative of (18) along the trajectories of the e_1 subsystem is

$$\begin{aligned} \dot{V}_1(\boldsymbol{e}_1) &= \boldsymbol{e}_1^{\mathrm{T}} \dot{\boldsymbol{e}}_1 \\ &= \begin{bmatrix} \tilde{\boldsymbol{p}}_p^{\mathrm{T}} & \tilde{\psi} \end{bmatrix} \begin{bmatrix} \tilde{\boldsymbol{v}} - \boldsymbol{S}(r)\tilde{\boldsymbol{p}}_p \\ \tilde{r} \end{bmatrix}. \end{aligned} \tag{19}$$

It is now utilized that

$$\tilde{\boldsymbol{p}}_p^{\mathrm{T}} \boldsymbol{S}(r) \tilde{\boldsymbol{p}}_p = \begin{bmatrix} \tilde{N}_p & \tilde{E}_p & \tilde{D}_p \end{bmatrix} \begin{bmatrix} 0 & -r & 0 \\ r & 0 & 0 \\ 0 & 0 & 0 \end{bmatrix} \begin{bmatrix} \tilde{N}_p \\ \tilde{E}_p \\ \tilde{D}_p \end{bmatrix} = 0 \;\; \forall \;\; \tilde{\boldsymbol{p}}_p, r \tag{20}$$

which reduces (19) to

$$\begin{aligned} \dot{V}_1(\boldsymbol{e}_1) &= \begin{bmatrix} \tilde{\boldsymbol{p}}_p^{\mathrm{T}} & \tilde{\psi} \end{bmatrix} \begin{bmatrix} \tilde{\boldsymbol{v}} \\ \tilde{r} \end{bmatrix} \\ &= \boldsymbol{e}_1^{\mathrm{T}} \boldsymbol{e}_2 \,. \end{aligned} \tag{21}$$

Now consider $\boldsymbol{e}_2$ from (12), and (13), and choose the desired velocity as

$$\boldsymbol{\nu}_d = \boldsymbol{\nu}_v + \boldsymbol{K}_1 \boldsymbol{e}_1 \tag{22}$$

where $\boldsymbol{\nu}_v$ can be generated by, e.g., a reference model, and $\boldsymbol{K}_1 \boldsymbol{e}_1$ is a stabilizing function.

Combining (12) and (22) gives $\boldsymbol{e}_2 = \boldsymbol{\nu} - \boldsymbol{\nu}_v - \boldsymbol{K}_1 \boldsymbol{e}_1$. As such, when $\boldsymbol{\nu} \to \boldsymbol{\nu}_v$ (as will be shown later in the proof), then $\boldsymbol{e}_2 \to -\boldsymbol{K}_1 \boldsymbol{e}_1$. In the case $\boldsymbol{\nu} = \boldsymbol{\nu}_v$,

$$\dot{V}_1 = -\boldsymbol{e}_1^{\mathrm{T}} \boldsymbol{K}_1 \boldsymbol{e}_1 \leq -\lambda_{min}(\boldsymbol{K}_1) \boldsymbol{e}_1^{\mathrm{T}} \boldsymbol{e}_1 \tag{23}$$

where $\lambda_{min}(\boldsymbol{K}_1)$ is the smallest eigenvalue of $\boldsymbol{K}_1$. By Khalil (2002, Thm.4.10), the equilibrium point $\boldsymbol{e}_1 = 0$ is globally exponentially stable in the state space of $\boldsymbol{e}_1$.

Step 2: Now consider (14), which has time derivative

$$\dot{\bar{\boldsymbol{e}}}_2 = \boldsymbol{M}^{-1} \left(-\boldsymbol{D}_l \boldsymbol{\nu} - \boldsymbol{D}_n(\boldsymbol{\nu}) \boldsymbol{\nu} + \boldsymbol{g}(\boldsymbol{\eta}) + \boldsymbol{\tau} + \boldsymbol{\tau}_c \right) - \dot{\boldsymbol{\nu}}_v \tag{24}$$

where $\dot{\boldsymbol{\nu}}_v = \begin{bmatrix} \dot{u}_v & \dot{v}_v & \dot{w}_v & \dot{r}_v \end{bmatrix}$ are the virtual accelerations, and introduce a second Lyapunov function candidate

$$V_2(\boldsymbol{e}_1, \bar{\boldsymbol{e}}_2) = V_1(\boldsymbol{e}_1) + \frac{1}{2} \bar{\boldsymbol{e}}_2^{\mathrm{T}} \boldsymbol{M} \bar{\boldsymbol{e}}_2 \geq 0 \;\; \forall \;\; \boldsymbol{e}_1, \bar{\boldsymbol{e}}_2. \tag{25}$$

The time derivative of V_2 along the trajectories of the $\boldsymbol{e}_1, \bar{\boldsymbol{e}}_2$ subsystem is

$$\dot{V}_2(\boldsymbol{e}_1, \bar{\boldsymbol{e}}_2) = \dot{V}_1(\boldsymbol{e}_1) + \bar{\boldsymbol{e}}_2^{\mathrm{T}} \boldsymbol{M} \dot{\bar{\boldsymbol{e}}}_2 \,. \tag{26}$$

Inserting (24) gives

$$\begin{aligned} \dot{V}_2(\boldsymbol{e}_1, \bar{\boldsymbol{e}}_2) = &- \boldsymbol{e}_1^{\mathrm{T}} \boldsymbol{K}_1 \boldsymbol{e}_1 + \boldsymbol{e}_1^{\mathrm{T}} \bar{\boldsymbol{e}}_2 \\ &+ \bar{\boldsymbol{e}}_2^{\mathrm{T}} (-\boldsymbol{M} \dot{\boldsymbol{\nu}}_v - \boldsymbol{D}_l \boldsymbol{\nu} - \boldsymbol{D}_n(\boldsymbol{\nu}) \boldsymbol{\nu} + \boldsymbol{g}(\boldsymbol{\eta}) + \boldsymbol{\tau} + \boldsymbol{\tau}_c^b). \end{aligned} \tag{27}$$

The model uncertainties, i.e., the parameters of the matrices $\boldsymbol{M}$, $\boldsymbol{D}_l$ and $\boldsymbol{D}_n$, the gravitational force $\boldsymbol{g}(\boldsymbol{\eta})$ and the current disturbance $\boldsymbol{\tau}_c^b$, are now represented by a constant vector $\boldsymbol{\Psi} \in \mathbb{R}^{15}$. The known signals of the virtual acceleration, the measured velocities, and the measured positions and attitudes are represented by a matrix $\boldsymbol{\Phi} \in \mathbb{R}^{15\times4}$ so that

$$\boldsymbol{\Phi}^{\mathrm{T}}(\dot{\boldsymbol{\nu}}_v, \boldsymbol{\nu}, \boldsymbol{\eta}) \boldsymbol{\Psi} = \boldsymbol{M} \dot{\boldsymbol{\nu}}_v + \boldsymbol{D}_l \boldsymbol{\nu} + \boldsymbol{D}_n(\boldsymbol{\nu}) \boldsymbol{\nu} + \boldsymbol{g}(\boldsymbol{\eta}) - \boldsymbol{J}^{\mathrm{T}}(\boldsymbol{\eta}) \boldsymbol{\tau}_c. \tag{28}$$

The ocean current force disturbance is estimated in the NED frame, as this is assumed constant, by including the rotation matrix $\boldsymbol{J}(\boldsymbol{\eta})$ in $\boldsymbol{\Phi}$ and the current force $\boldsymbol{\tau}_c$ in $\boldsymbol{\Psi}$. This reduces (27) to

$$\dot{V}_2(\boldsymbol{e}_1, \bar{\boldsymbol{e}}_2, t) = -\boldsymbol{e}_1^{\mathrm{T}} \boldsymbol{K}_1 \boldsymbol{e}_1 + \boldsymbol{e}_1^{\mathrm{T}} \bar{\boldsymbol{e}}_2 + \bar{\boldsymbol{e}}_2^{\mathrm{T}} (\boldsymbol{\tau} - \boldsymbol{\Phi}^{\mathrm{T}} \boldsymbol{\Psi}). \tag{29}$$

Inserting (15) gives

$$\dot{V}_2(\boldsymbol{e}_1, \bar{\boldsymbol{e}}_2) = -\boldsymbol{e}_1^{\mathrm{T}} \boldsymbol{K}_1 \boldsymbol{e}_1 - \bar{\boldsymbol{e}}_2^{\mathrm{T}} \boldsymbol{K}_2 \bar{\boldsymbol{e}}_2 + \bar{\boldsymbol{e}}_2^{\mathrm{T}} \boldsymbol{\Phi}^{\mathrm{T}} \tilde{\boldsymbol{\Psi}} \tag{30}$$

where $\tilde{\boldsymbol{\Psi}} \triangleq \hat{\boldsymbol{\Psi}} - \boldsymbol{\Psi}$.

Step 3: Now consider a third Lyapunov function candidate

$$V_3(\boldsymbol{e}_1, \bar{\boldsymbol{e}}_2, \tilde{\boldsymbol{\Psi}}) = V_2 + \frac{1}{2} \tilde{\boldsymbol{\Psi}}^{\mathrm{T}} \boldsymbol{\Gamma}^{-1} \tilde{\boldsymbol{\Psi}} \;\; \geq 0 \; \forall \, \boldsymbol{e}_1, \bar{\boldsymbol{e}}_2, \tilde{\boldsymbol{\Psi}} \,. \tag{31}$$

The time derivative of (31) along the trajectories of the $\boldsymbol{e}_1, \bar{\boldsymbol{e}}_2, \tilde{\boldsymbol{\Psi}}$ system is

$$\dot{V}_3(\boldsymbol{e}_1, \bar{\boldsymbol{e}}_2, \tilde{\boldsymbol{\Psi}}) = -\boldsymbol{e}_1^{\mathrm{T}} \boldsymbol{K}_1 \boldsymbol{e}_1 - \bar{\boldsymbol{e}}_2^{\mathrm{T}} \boldsymbol{K}_2 \bar{\boldsymbol{e}}_2 + \tilde{\boldsymbol{\Psi}}^{\mathrm{T}} (\boldsymbol{\Phi} \bar{\boldsymbol{e}}_2 + \boldsymbol{\Gamma}^{-1} \dot{\tilde{\boldsymbol{\Psi}}}). \tag{32}$$

It is assumed (Assumptions 5 and 6) that the vehicle's parameters, the gravitational force, and the current disturbance forces are constant, hence $\dot{\boldsymbol{\Psi}} = 0$ and thus $\dot{\tilde{\boldsymbol{\Psi}}} = \dot{\hat{\boldsymbol{\Psi}}}$. Inserting the adaptation law from (16) reduces (32) to

$$\dot{V}_3(\boldsymbol{e}_1, \bar{\boldsymbol{e}}_2, \tilde{\boldsymbol{\Psi}}) = -\boldsymbol{e}_1^{\mathrm{T}} \boldsymbol{K}_1 \boldsymbol{e}_1 - \bar{\boldsymbol{e}}_2^{\mathrm{T}} \boldsymbol{K}_2 \bar{\boldsymbol{e}}_2 \,. \tag{33}$$

This implies that $V_3(t) \leq V_3(0)$ and that the origin of the system is stable (Khalil, 2002, Th. 4.1). By Khalil (2002, Th. 8.4), all trajectories of the $\boldsymbol{e}_1, \bar{\boldsymbol{e}}_2, \tilde{\boldsymbol{\Psi}}$ system are bounded. Furthermore, also by Khalil (2002, Th. 8.4), all trajectories converge to $\dot{V}_3 = 0 \implies \boldsymbol{e}_1 = \bar{\boldsymbol{e}}_2 = 0$ for all initial values. □

3.3. Parameter convergence

The adapted parameters, $\hat{\boldsymbol{\Psi}}$, stop converging if the error variable $\bar{\boldsymbol{e}}_2$ reaches zero due to the structure of the update law (16). As shown in the previous section, $\bar{\boldsymbol{e}}_2 \to 0$. Convergence of $\tilde{\boldsymbol{\Psi}}$ to zero (and thus global asymptotic stability for the whole state space $\mathcal{E} = \begin{bmatrix} \boldsymbol{e}_1^{\mathrm{T}} & \bar{\boldsymbol{e}}_2^{\mathrm{T}} & \tilde{\boldsymbol{\Psi}}^{\mathrm{T}} \end{bmatrix}^{\mathrm{T}}$), requires $\boldsymbol{\Phi}\boldsymbol{\Phi}^{\mathrm{T}}$ to be *persistently exciting* (PE).

Corollary 1 (*GAS and PE*). *If there exists a time $T > 0$ and a constant $\mu > 0$ such that*

$$\int_t^{t+T} \boldsymbol{\Phi}(\tau)\boldsymbol{\Phi}^{\mathrm{T}}(\tau)\, d\tau \geq \mu \;\; \forall\, t \in \mathbb{R}_{\geq 0}, \tag{34}$$

the origin of the $\mathcal{E} = \begin{bmatrix} \boldsymbol{e}_1^{\mathrm{T}} & \bar{\boldsymbol{e}}_2^{\mathrm{T}} & \tilde{\boldsymbol{\Psi}}^{\mathrm{T}} \end{bmatrix}^{\mathrm{T}}$ system is globally asymptotically stable.

Proof. As V_3 is a quadratic function in $\mathcal{E}$, there trivially exist two functions $\alpha_1(\|\mathcal{E}\|), \alpha_2(\|\mathcal{E}\|) \in K_\infty$ such that

$$\alpha_1(\cdot) \leq V_3(\boldsymbol{e}_1, \bar{\boldsymbol{e}}_2, \tilde{\boldsymbol{\Psi}}) \leq \alpha_2(\cdot)\,. \tag{35}$$

Now introduce the continuous function $V^*(\boldsymbol{e}_1, \bar{\boldsymbol{e}}_2)$ satisfying

$$\dot{V}_3(\boldsymbol{e}_1, \bar{\boldsymbol{e}}_2, \tilde{\boldsymbol{\Psi}}) \leq V^*(\boldsymbol{e}_1, \bar{\boldsymbol{e}}_2)\,, \tag{36}$$

e.g.,

$$V^*(\boldsymbol{e}_1, \bar{\boldsymbol{e}}_2) = -\boldsymbol{e}_1^{\mathrm{T}}\boldsymbol{K}_1\boldsymbol{e}_1 - \bar{\boldsymbol{e}}_2^{\mathrm{T}}\boldsymbol{K}_2\bar{\boldsymbol{e}}_2\,. \tag{37}$$

Consider the function

$$W(\boldsymbol{\Psi}, \bar{\boldsymbol{e}}_2) = -\tilde{\boldsymbol{\Psi}}^{\mathrm{T}}\boldsymbol{\Phi}\bar{\boldsymbol{e}}_2 \tag{38}$$

which is Lipschitz continuous, since all its dependencies are Lipschitz continuous. The time derivative of (38) along the trajectory of the closed-loop system is

$$\begin{aligned} \dot{W} &= -\dot{\tilde{\boldsymbol{\Psi}}}^{\mathrm{T}}\boldsymbol{\Phi}\bar{\boldsymbol{e}}_2 - \tilde{\boldsymbol{\Psi}}^{\mathrm{T}}\dot{\boldsymbol{\Phi}}\bar{\boldsymbol{e}}_2 - \tilde{\boldsymbol{\Psi}}^{\mathrm{T}}\boldsymbol{\Phi}\dot{\bar{\boldsymbol{e}}}_2 \\ &= -\tilde{\boldsymbol{\Psi}}^{\mathrm{T}}\boldsymbol{\Phi}\boldsymbol{\Phi}^{\mathrm{T}}\tilde{\boldsymbol{\Psi}} + \bar{\boldsymbol{e}}_2^{\mathrm{T}}\left[\boldsymbol{\Gamma}\boldsymbol{\Phi}^{\mathrm{T}}\boldsymbol{\Phi}\bar{\boldsymbol{e}}_2 - \dot{\boldsymbol{\Phi}}^{\mathrm{T}}\tilde{\boldsymbol{\Psi}} + \boldsymbol{K}_2^{\mathrm{T}}\boldsymbol{\Phi}^{\mathrm{T}}\boldsymbol{\Psi}\right]. \end{aligned} \tag{39}$$

On the set

$$\bar{M} \triangleq \left\{\mathcal{E} \in \boldsymbol{B} : V^*(\boldsymbol{e}_1, \bar{\boldsymbol{e}}_2) = 0\right\} \tag{40}$$

where

$$\boldsymbol{B} \triangleq \left\{\mathcal{E} \in \mathbb{R}^{23} \;:\; \|\mathcal{E}\| < \bar{R}\right\} \tag{41}$$

and $\bar{R}$ is some positive constant, (39) is non-zero definite if $\tilde{\boldsymbol{\Psi}}^{\mathrm{T}}\boldsymbol{\Phi}\boldsymbol{\Phi}^{\mathrm{T}}\tilde{\boldsymbol{\Psi}} \geq \mu\tilde{\boldsymbol{\Psi}}^{\mathrm{T}}\tilde{\boldsymbol{\Psi}} > 0$ can be ensured. That is, the signal $\boldsymbol{\Phi}\boldsymbol{\Phi}^{\mathrm{T}}$ must be *persistently exciting*; there exist a time $T > 0$ and a constant $\mu > 0$ such that Loría et al. (2005)

$$\int_t^{t+T} \boldsymbol{\Phi}(\tau)\boldsymbol{\Phi}^{\mathrm{T}}(\tau)\, \mathrm{d}\tau \geq \mu \;\; \forall t \in \mathbb{R}_{\geq 0} \tag{42}$$

which is assumed in (34). Thus, by Ioannou and Sun (2012, Corollary 4.3.1), $\hat{\boldsymbol{\Psi}} \to \boldsymbol{\Psi}$ exponentially fast and by Matrosov's Theorem (Matrosov, 1962), $\mathcal{E} = 0$ is a globally asymptotically stable equilibrium point. □

4. Results

A simulation study was conducted to illustrate the theoretical results in an ideal framework, and in order to compare the proposed controller with other, similar controllers. An experimental trial was thereafter conducted to test the real-world performance. Performing the real-world experiments obviates the need for a simulation study using a more sophisticated simulation model.

4.1. Simulation without persistency of excitation

The control plant model from (1) and (2), as well as the proposed control algorithm, was implemented in FhSim, a software platform and framework for mathematical modeling and numerical simulation with a focus on marine applications (Reite et al., 2014) and Su et al. (2019). All necessary measurements were assumed available, i.e., the controller has full state feedback from the control plant model given by (1) and (2). The parameters of the control plant model are given in Appendix A. The controller parameters, the matrix $\boldsymbol{\Phi}$, and the estimated parameter vector $\boldsymbol{\Psi}$ used in the simulations are given in Appendix B.

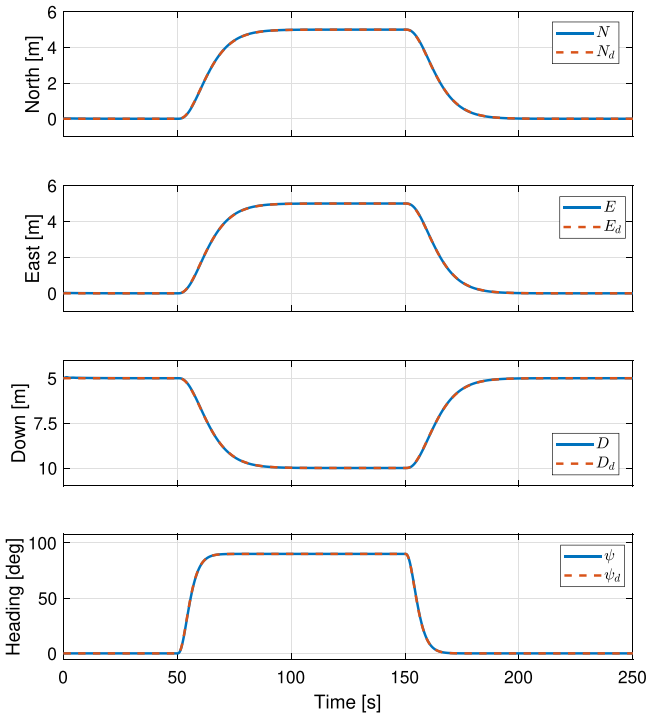

Fig. 1. The positions and heading during the simulation. In descending order: North, East, Down and Heading angle. The red lines are the desired positions and heading angle, while the blue line is the ROV's position and heading angle. (For interpretation of the references to color in this figure legend, the reader is referred to the web version of this article.)

The first simulation scenario considers station keeping at a given point with a given heading for 50 s. The vehicle was then commanded to move to a different point and change the heading before moving back to the original point and heading.

The virtual velocities and accelerations in the vectors $\boldsymbol{\nu}_v$ and $\dot{\boldsymbol{\nu}}_v$ were generated by passing the desired positions and attitude through 3rd order reference models. For a single degree of freedom, the reference model takes the form

$$\boldsymbol{\eta}_d(s) = \frac{\omega^3}{s^3 + (2\zeta + 1)\omega s^2 + (2\zeta + 1)\omega s + \omega^3}\eta_r \tag{43}$$

where $\boldsymbol{\eta}_d \in \mathbb{R}^3$ contains the filtered position, velocity and acceleration and η_r is the input to the reference model, i.e., the desired position or attitude. The natural damping $\zeta = 1$ and the values for the natural frequencies were chosen as $\omega = 0.2$ for N, E and D and $\omega = 0.5$ for ψ. Generating $\boldsymbol{\nu}_v$ with a reference model ensures smooth trajectories and may help reduce overshoots when changing positions and attitude. This is crucial when operating inside a fish cage, as hitting, e.g., the net wall may lead to holes in the net through which fish may escape. The ocean current disturbance force was set to $\boldsymbol{\tau}_c = \begin{bmatrix}50 & 50 & 0 & 0\end{bmatrix}^{\mathrm{T}}$. The initial position of the ROV was $\boldsymbol{\eta}_0 = \begin{bmatrix}0 & 0 & 5 & 0\end{bmatrix}^{\mathrm{T}}$ which was also the initial desired position fed to the controller for the first 50 s of the simulation. The ROV was then commanded to simultaneously move 5 meters North, 5 meters East, 5 meters Down and change the heading to $\psi = 90°$ and hold this position and attitude for 100 s before returning to the original position and heading.

Fig. 1 shows the positions, N, E, D, and the attitude, ψ, of the ROV during one simulation. It is clear that the presented controller implemented on the control plant model is able to perform the operation under the influence of ocean currents, and that the controller successfully moves the ROV to its new reference when a new setpoint is given. From Fig. 2 it can be seen that the calculated control forces are smooth and within a feasible range.

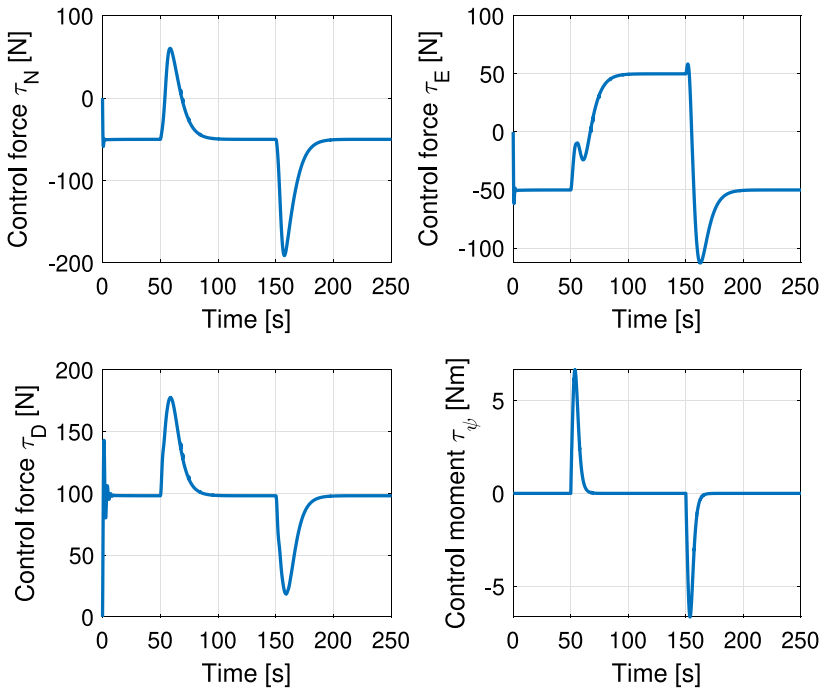

Fig. 2. The calculated control forces and moment in the four degrees of freedom during the simulation without persistency of excitation.

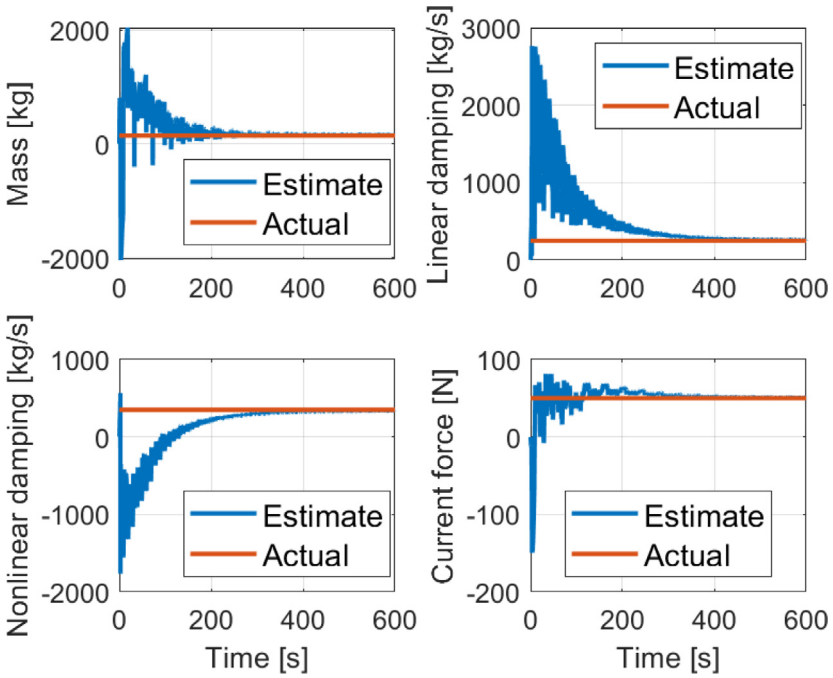

Fig. 3. The estimated parameters and current disturbance in the North degree of freedom with a PE signal. Simulation results.

4.2. Simulation with persistency of excitation

To demonstrate the parameter estimation properties of the proposed control law, a persistently exciting reference signal was applied in the N direction. The other degrees of freedom are set to constant values and hence, the parameters associated with these degrees of freedom are irrelevant. The N direction is associated with four parameters, i.e., the mass, linear and nonlinear damping coefficients, and the current force. To achieve fast convergence of the estimated parameters, the adaptation gains affecting the N direction were increased. These gains are shown in Appendix B. The parameter ω of the 3rd-order reference model (43) was changed to $\omega = 1$ so that the desired velocity and acceleration were larger. This in turn ensured that the velocity and acceleration signals in $\boldsymbol{\Phi}$ were larger and that the adaptation was faster. The controller gains $\boldsymbol{K}_1$ and $\boldsymbol{K}_2$ were as in the previous simulation. The PE reference signal consisted of a sum of two square pulse signals, both with an amplitude of 8 meters and periods of 40 and 20 seconds, respectively. This particular signal was chosen since it is assumed, even after passing through the reference models, to contain the required frequency content to estimate the unknown parameters. In general, for linear systems, parameter convergence of p parameters requires at least $p/2$ sinusoids in the reference signal. For nonlinear

Table 1
Numerical comparison of simulation results using three different controllers.

	Proposed		Dist. adapt		Int. aug	
	$\|\|e\|\|$	IAE	$\|\|e\|\|$	IAE	$\|\|e\|\|$	IAE
North error	0.37	10.99	0.37	11.65	2.96	71.63
East error	0.38	11.22	0.39	11.66	5.91	124.64
Down error	0.42	11.84	0.43	12.18	7.03	183.48
ψ error	7.10	97.66	7.28	100.66	14.52	231.67

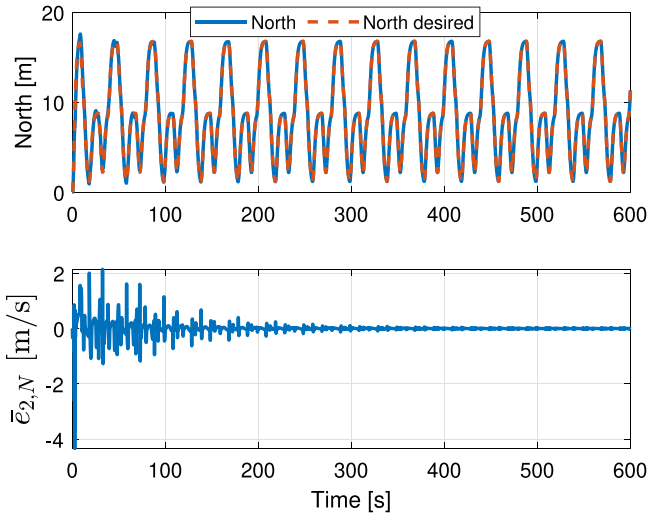

Fig. 4. The position and error signals in the North degree of freedom during simulation with a PE signal. Simulation results.

systems, however, it is unclear how many sinusoids are necessary in the reference signal (Slotine & Li, 1991, Ch. 8). Since a square pulse signal contains an infinite number of sinusoids, it was considered a reasonable candidate reference signal for parameter estimation in this case.

As seen in Fig. 3, the estimates of the system parameters in the North degree of freedom successfully converged to their actual values. Furthermore, Fig. 4 shows that the controller is successfully able to follow a time-varying reference signal. However, Fig. 5 shows that the calculated control signal in the North degree of freedom is very large. This is caused by the large initial error of the error variable $\bar{e}_2$, which can be seen in Fig. 4, and the large adaptation gains which causes large transients in the estimated parameters at the beginning of the simulation. Furthermore, the choice of parameters for the North degree of freedom reference model leads to a large virtual acceleration, $\dot{u}_v$ and a large desired velocity u. The control signal τ_N from Fig. 5 will not be feasible in a real-world setting. However, the goal of this simulation is to demonstrate that the estimated parameters converge to the actual values, not to prepare the controller for implementation in a real-world trial.

4.3. Comparison with similar controllers

The proposed controller adapts both the uncertain system parameters and the unknown external disturbances arising from ocean currents and gravitational forces. It is of interest to investigate how the proposed controller compares to similar controllers. Hence, simulations were performed using a controller that only adapts the unknown external disturbances, and using a controller with no adaptation but with integral augmentation (as in Fossen (2011, Ch.13.3.5)). The control objective, ocean currents and reference model parameters when using these controllers are as in Section 4.1.

4.3.1. External disturbance adaptation

This controller is realized by using (15) and (16), with the coefficients of $\boldsymbol{\Gamma}$ in (16) corresponding to the parameter estimates set to zero. The coefficients corresponding to the external disturbances – i.e., g_z, τ_c^x and τ_c^y – are kept at the same values as in the simulation with full adaptation. The controller parameters are found in Appendix B.

4.3.2. Integral augmentation

This controller is realized using

$$\boldsymbol{\tau}_I = -\boldsymbol{K}_2\bar{\boldsymbol{e}}_2 - \boldsymbol{e}_1 - \boldsymbol{K}_I \int_0^t \boldsymbol{e}_1(\tau)\mathrm{d}\tau\,, \tag{44}$$

where $\boldsymbol{K}_I = \boldsymbol{K}_I^{\mathrm{T}} \in \mathbb{R}^{4\times4} > \boldsymbol{0}$ is a diagonal matrix of integral gains. Apart from the integral term, the controller in (44) is equal to (15), i.e., they have the same proportional and derivative terms. The main difference is that the external disturbance is compensated by integrating the position error in the vessel parallel coordinate system when using (44). The proposed controller in this paper depends on an integral of both the position and velocity error when building compensation. This may lead to less accurate compensation if the measurements are contaminated with noise since two signals are required in the proposed method (Fossen, 2011, pp. 475). A pure integral action, however, is sensitive to the chosen control gain, and may suffer if the control design is not performed with great care (Skjetne & Fossen, 2004).

4.3.3. Simulation results using similar controllers

Figs. 6 and 7 respectively show the error signal and the calculated control forces for the three different controllers. Furthermore, Table 1 shows the 2-norm of the error in each degree of freedom as well as the integrated absolute error (IAE) in each degree of freedom for all three controllers. From Figs. 6 and 7 and Table 1, it can be seen that the proposed controller and the disturbance adapting controller both have a lower error norm and a lower IAE than the controller with integral augmentation. The proposed controller has slightly lower error norm and IAE than the pure disturbance-adapting controller in the numerical comparison.

Considering the moderate increase in performance at the cost of introducing more tuning parameters when using the proposed controller, one may ask whether the parameter adaptation is necessary. In this simulation study, all parameters where kept constant, and the velocity of the ROV was quite low, i.e., the linear and nonlinear damping effects are small and thus the effects of the parameter adaptation are close to negligible. This may not be the case in a real-world scenario and adaptation may prove beneficial in these cases.

4.4. Real-world experiments

Three different scenarios were tested in the field trial. Scenario 1 concerned dynamic positioning, Scenario 2 introduced setpoint changes in all controlled DOFs, and Scenario 3 tested the parameter estimation capabilities of the proposed controller. The ROV was submerged inside a fish cage containing several hundred tons of live Atlantic salmon (*Salmo salar*). The parameters of the ROV such as mass and damping coefficients are not known with certainty, hence the initial conditions for all estimated parameters were set to zero. The controller parameters were tuned during the field trial, and are given in Appendix B.

4.4.1. The Argus Mini ROV and existing control system

The vehicle used in the field trial is an Argus Mini ROV, a 90 kg Observation-class ROV (Argus Remote Systems, 2021). The Argus Mini has 4 thrusters in the horizontal plane and 2 thrusters in the vertical plane. It is slightly positively buoyant and passively stabilized in roll and pitch.

The ROV is controlled through a graphical user interface named Aqueous, implemented in JavaScript/React. This interface allows the operator to turn on/off manual control and DP, and set the desired positions for DP. The operator can view the ROV states – i.e., the positions and velocities – as well as the camera feed from the ROV. The Aqueous interface communicates with the low-level control algorithms,

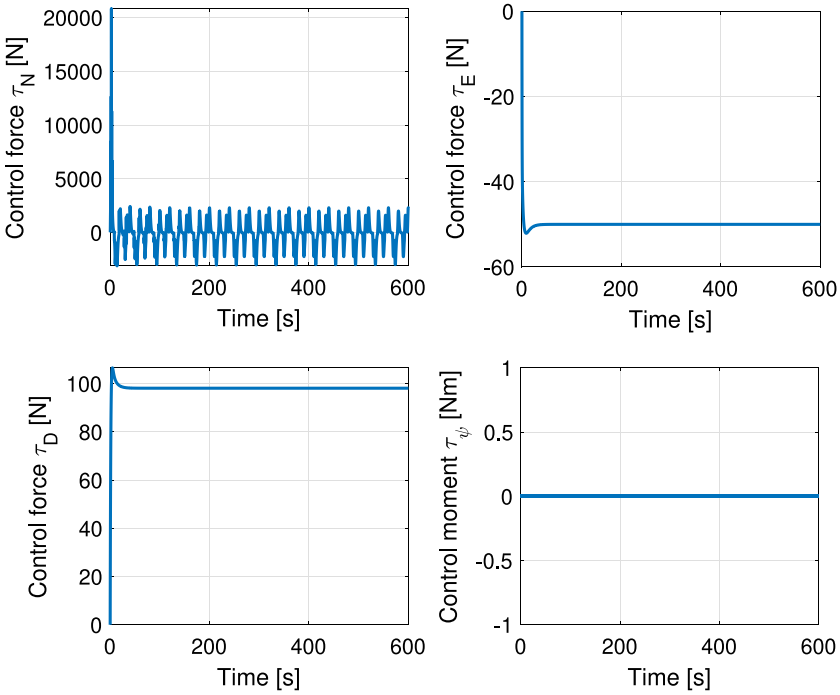

Fig. 5. The control forces and moment in the four degrees of freedom during simulation with persistency of excitation.

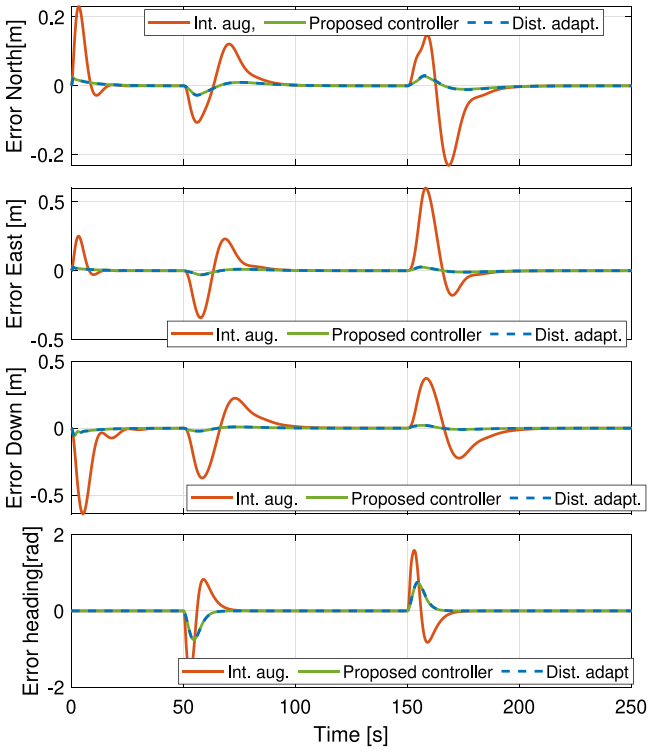

Fig. 6. Comparison of errors using the proposed controller (green), a controller with only disturbance adaptation (blue dashed) and a controller using integral augmentation (red). (For interpretation of the references to color in this figure legend, the reader is referred to the web version of this article.)

implemented in C++ in the software framework FhSim, through the Inter-Module Communication Protocol (IMC) (Martins et al., 2009). FhSim sends a normalized command (between −1 and 1) to each individual thruster via a serial connection from the topside computer. As such, the calculated desired forces and moments from the controller must be allocated to specific thrusters. This thrust allocation is given in Appendix A. Each thruster on the ROV can, according to the manufacturer, produce a maximum thrust of approximately 117 N in the positive direction and approximately 95 N in the negative direction. The rate of change for the thrusters is limited by a rate slew limiter, also given in Appendix A.

It should be noted that during the development of the proposed controller, the thruster configuration and thruster rate limitations were intentionally left out. As will be shown, the proposed controller was still able to achieve the desired objectives even in the presence of these limitations.

The Argus Mini is equipped with a depth sensor, magnetic compass, a DVL for velocity measurements, and a USBL acoustic transmitter for underwater positioning. The ROV control system contains an Extended Kalman Filter that provides the controller with estimates of the N, E and D positions, the heading angle ψ, the velocities u, v and w, and the yaw rate r.

The Argus Mini ROV is already equipped with a pre-tuned nonlinear PD controller with bias estimation for DP purposes (hereafter referred to as "the PD controller"). This controller is taken from Loria et al. (2000) and has the form

$$\boldsymbol{\tau}_{PD} = -\boldsymbol{J}(\psi)^{\mathrm{T}}\boldsymbol{K}_p\boldsymbol{e} - \boldsymbol{K}_d\hat{\boldsymbol{\nu}} - \boldsymbol{J}(\psi)^{\mathrm{T}}\hat{\boldsymbol{b}}, \quad \boldsymbol{e} = \hat{\boldsymbol{\eta}} - \boldsymbol{\eta}_d\,, \tag{45}$$

where $\boldsymbol{K}_p \in \mathbb{R}^{4\times4}$ and $\boldsymbol{K}_d \in \mathbb{R}^{4\times4}$ are gain matrices, $\boldsymbol{J}(\psi)$ is as in (3), and $\hat{\boldsymbol{\eta}}$, $\hat{\boldsymbol{\nu}}$ and $\hat{\boldsymbol{b}}$ are position, velocity, and bias estimates provided by an Extended Kalman Filter (EKF). The authors have, in earlier trials, experienced that the bias estimation is very sensitive to measurement noise. To overcome this, the time constants of the bias estimates in the EKF have all been set to 100 s, which in this case is quite slow. As a consequence, the integral effect of this controller is also slow. The implemented PD controller further assumes $\dot{\boldsymbol{\eta}}_d = 0$, which is not necessarily the case. To illustrate the differences between the already implemented controller and the proposed controller, experiments were conducted with both controllers.

4.4.2. Scenario 1: Results using the proposed controller

Prior to enabling the dynamic positioning control, the ROV was manually controlled by the operator and brought to a desired position.

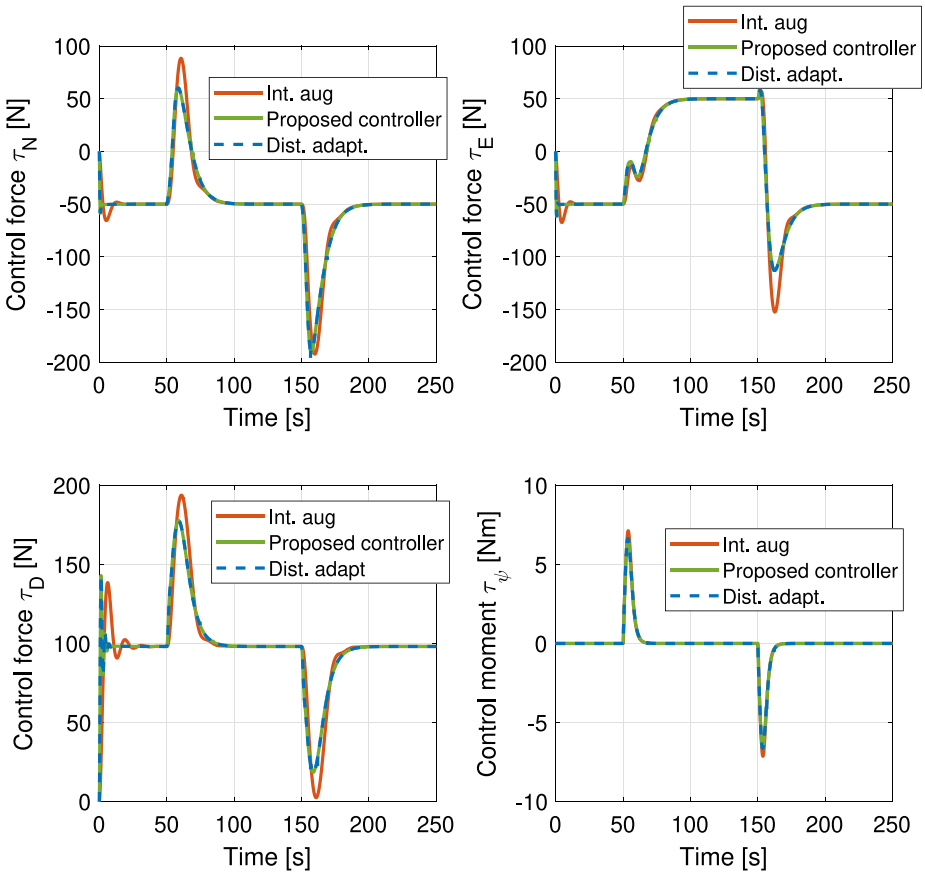

Fig. 7. Comparison of calculated control forces using the proposed controller (green), a controller with only disturbance adaptation (blue dashed) and a controller using integral augmentation (red). (For interpretation of the references to color in this figure legend, the reader is referred to the web version of this article.)

The calculated force from the DP controller was set to zero while DP was off. When the DP-mode was activated, the last position and attitude estimates were fed as references to the DP controller to avoid sudden jumps. This explains why $\boldsymbol{\eta}_d = \boldsymbol{\eta}$ at the start, as shown in Fig. 8. Furthermore, Fig. 8 shows that the proposed controller, derived with several assumptions, was able to keep the ROV at the desired position and attitude when enabled. The calculated and applied control signals for this scenario are shown in Fig. 9. The applied control signals are equal to the calculated control signals (when DP is on), hence it is concluded the that calculated control signals are feasible.

All estimated parameters in the $\hat{\Psi}$ vector are shown in Fig. 10 as normalized values. The parameters related to the mass matrix (solid lines) are converging due to the fact that the variable $\dot{\boldsymbol{\nu}}_v = 0$ when doing DP. Parameter drift caused by measurement noise can be a problem when using adaptive control (Fossen & Fjellstad, 1995). It can be seen in Fig. 10 that the parameters related to the damping in the Down direction (dashed purple line and dashed dotted purple line) are somewhat drifting. This is due to some measurement noise in the heave velocity estimate and the fact that the actual velocity in this DOF is very small during DP. The other damping parameters in North, East and Heading and the estimated disturbances are not drifting or otherwise suffering from the influence of measurement noise, i.e., the applied Extended Kalman Filter is doing a sufficient job in filtering the measured signals. The presence of this drift, however, implies that a projection operator that ensures that the parameters stays within predefined bounds should be applied in the future (Ohrem et al., 2017).

4.4.3. Scenario 1: Results using the PD controller

In Fig. 11, the DP experiment was repeated with the PD controller. The PD controller was also able to keep the ROV at the desired position and attitude, but due to the slow integral action, the Down degree of freedom takes a long time to converge (longer than the time range shown in the figure). The control forces from this experiment are shown in Fig. 12. The calculated force using this controller is not set to zero prior to the DP being turned on (blue lines of Fig. 12). The effect of this is negligible as the integral part of the controller is dominated by the proportional and derivative part, which becomes clear by the rather immediate jump in the control signal when the DP is activated. The calculated and applied control forces from the PD controller seems to oscillate less compared to the control inputs from Fig. 9. This may imply that the actuators are experiencing less wear and tear when the PD controller is used.

Figs. 13 and 14 show the DP footprint plots for both the controllers in the N-E-plane. DP footprint plots are actual measurements of the vehicles DP station keeping performance in the actual environmental conditions and thruster configuration (DNV GL, 2015). The footprint plots show that the adaptive backstepping controller kept the ROV closer to the target reference, compared to the PD controller. Table 2 shows the mean Euclidean distance to the target position in the North-East plane, as well as the standard deviation of this distance. From this table, it can be seen that the proposed controller had a lower mean distance to the target and a lower standard deviation compared to the PD controller, but the applied control forces are more aggressive when using the proposed controller, which may lead to increased wear and tear on the ROVs thrusters. Furthermore, different tuning of the PD controller could perhaps lead to improved performance.

4.4.4. Scenario 2: Results using the proposed controller

In this scenario, the ROV was in DP-mode, but a change of desired positions and attitude was introduced. This function is quite useful for ROV operators, as they might be required to change the position and attitude of the ROV when performing, e.g., an inspection operation.

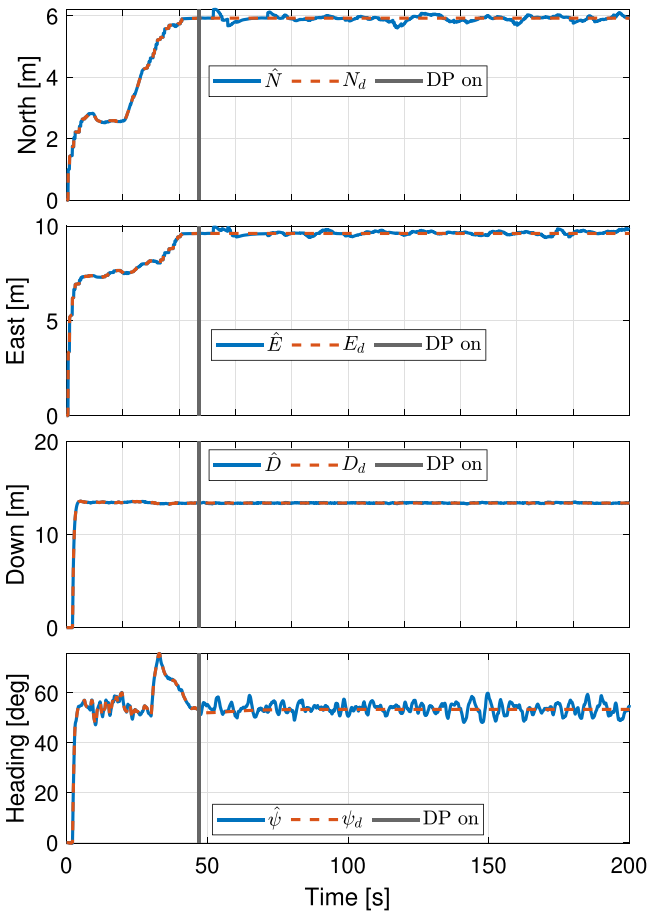

Fig. 8. Dynamic positioning using the proposed controller. In descending order: North, East, Down and Heading angle. Results from field trial.

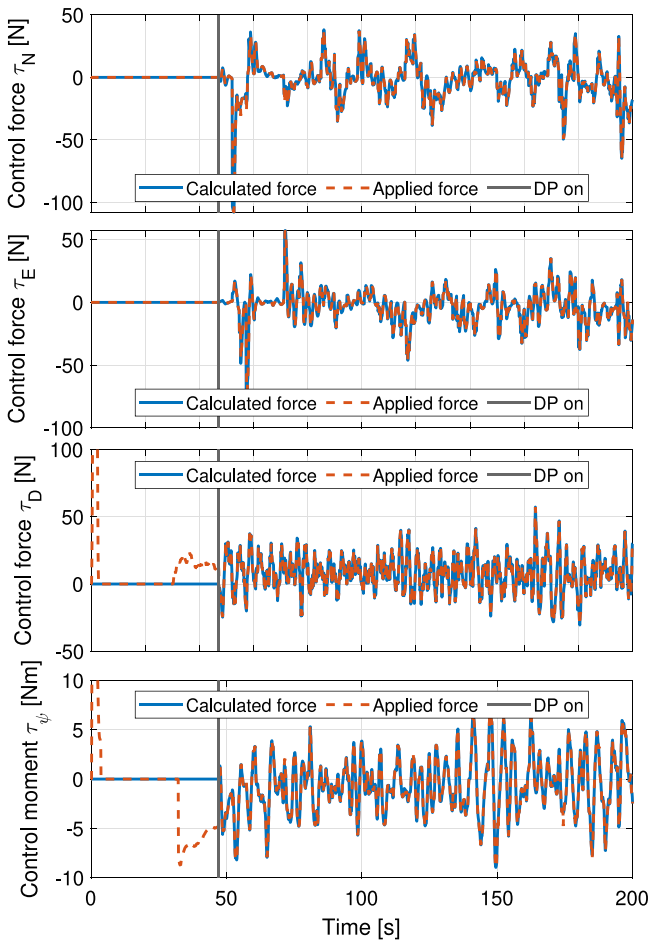

Fig. 9. The calculated and applied control forces during dynamic positioning using the proposed controller. The applied force prior to DP being turned on is the control signals sent from the operator. Results from field trial.

Table 2
Numerical comparison of the performance in the N-E plane of the proposed controller vs. the PD controller during Scenario 1. Results from field trial.

	Mean	Std. dev
Proposed controller	0.114 m	0.07 m
PD controller	0.38 m	0.23 m

In this experiment, when using the proposed controller, the ROV was commanded to move from its initial position to the position

$$\boldsymbol{\eta}_d = \begin{bmatrix} 6.5 & 9.8 & 13.2 & 49.3 \end{bmatrix}^{\mathrm{T}}$$

and hold this position. Then, after some time, the ROV was commanded to move to the setpoint

$$\boldsymbol{\eta}_d = \begin{bmatrix} 5.5 & 9.0 & 13.4 & 44.7 \end{bmatrix}^{\mathrm{T}}$$

and hold this position. The results are shown in Fig. 15 where it can be seen that the proposed controller was able to bring the ROV to the new setpoints with almost no overshoot. The reference model ensured that the steps were smooth. As the figures show, the position measurements in North and East, provided by the USBL, were affected by measurement noise which caused oscillations in the estimated positions. The calculated and applied control forces for this experiment are shown in Fig. 16

4.4.5. Scenario 2: Results using the PD controller

In Fig. 17 the results from a test using the PD controller are presented. Due to practical limitations during the experiments, a qualitatively but not quantitatively similar experiment was performed. The relative merits of the two control schemes in this scenario are therefore not quantified. The ROV was commanded to move from its initial position to the position

$$\boldsymbol{\eta}_d = \begin{bmatrix} 7.3 & 11.1 & 14.2 & 51.2 \end{bmatrix}^{\mathrm{T}}$$

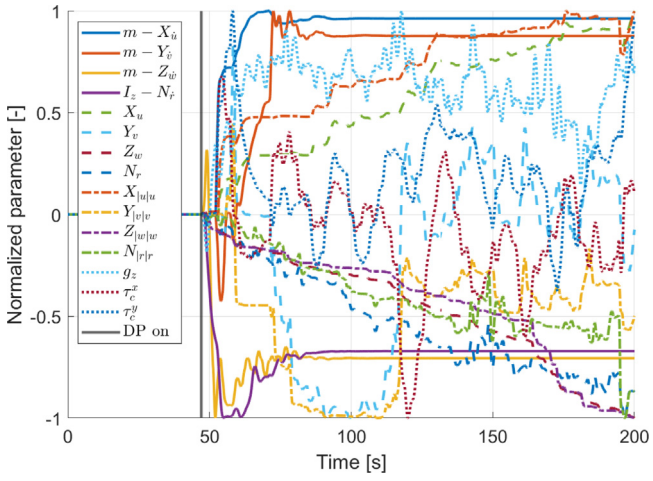

Fig. 10. All estimated parameters of the $\hat{\Psi}$ vector during the dynamic positioning trial. The parameters are normalized in order to represent them in the same figure.

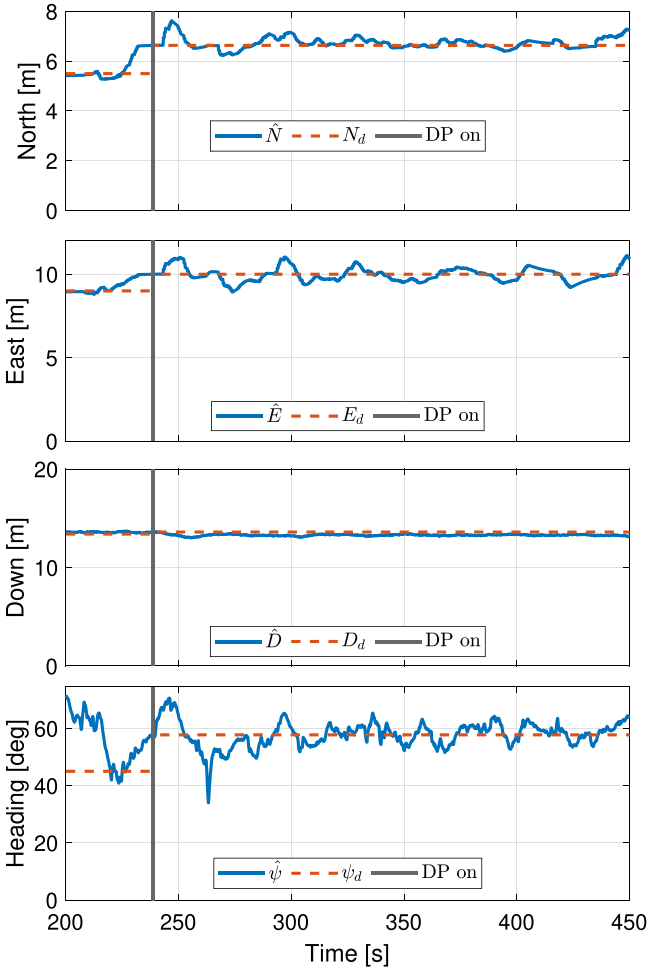

Fig. 11. Dynamic positioning using the PD controller. In descending order: North, East, Down and Heading angle. Results from field trial.

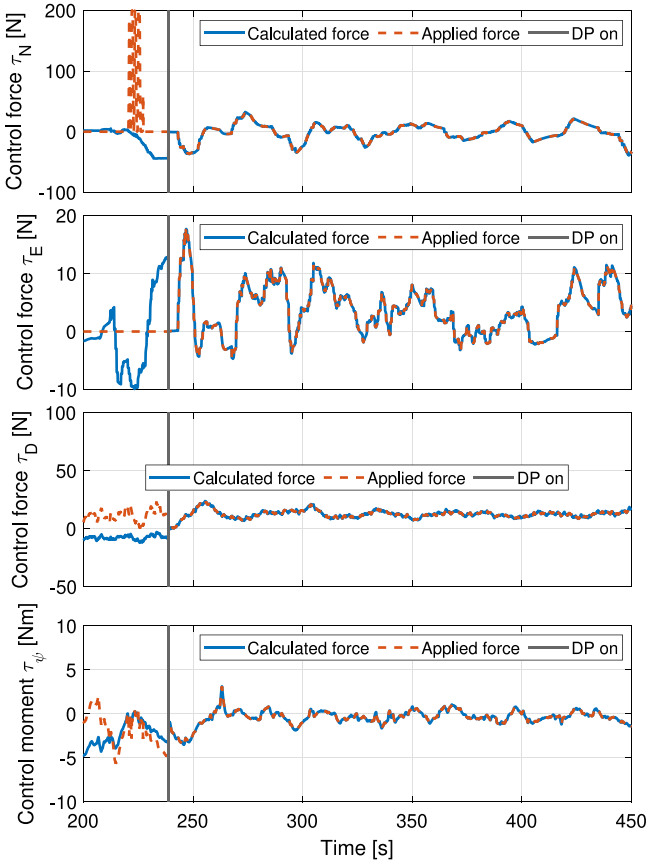

Fig. 12. The calculated and applied control forces during dynamic positioning using the PD controller. The applied force prior to DP being turned on is the control signals sent from the operator. Results from field trial.

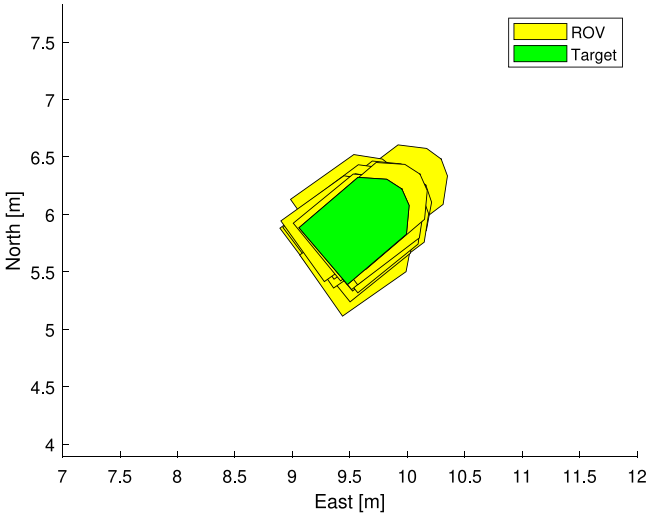

Fig. 13. DP footprint using the proposed controller, field trial.

and hold this position. Then, after some time, the ROV was commanded to move to the position

$$\boldsymbol{\eta}_d = \begin{bmatrix} 5.1 & 9.1 & 14.2 & 46.4 \end{bmatrix}^{\mathrm{T}}.$$

It can be seen from Fig. 17 that the PD controller was also able to bring the ROV to the new setpoints with very low overshoots. In Fig. 17, it is clear that the Down direction suffers from the slow integral action, as the state does not converge to the desired value in the time range shown in the figure. The same measurement noise from the USBL was present in this experiment, causing some oscillations in the estimated North and East positions. From Fig. 18 it is again apparent that the calculated and applied forces are less oscillatory with the PD controller compared to the proposed controller.

4.4.6. Scenario 3, results

An attempt was made to assess the parameter estimation capabilities of the proposed controller during the field trial. A persistently exciting signal consisting of a sum of two square pulse signals was given as a reference signal in the North direction. In the field trial, both square pulse signals had an amplitude of 8 meters and a bias of −4 meters. One signal had a period of 20 s and a width of 10 s, while the other had a period of 10 s and a width of 5 s. The PE signal was filtered through the reference model, and thus provided a smooth sinusoidal-like reference. Some of the richness is lost due to this filtering, but sufficient richness should remain in the reference signal for the parameter estimation.

The estimated parameters in the North degree of freedom are shown in Fig. 19. Here, it can be seen that the estimated mass and added mass did not converge to a realistic value, converging to a value with an unphysical negative sign. A negative value could have been avoided by, e.g., including a projection operator in the adaptation law (Ohrem et al., 2017). A projection operator ensures that the estimated parameters stays within some predefined bound, while maintaining the stability properties of the controller. Unfortunately, there was no time during the field trial to implement a projection operator. The linear

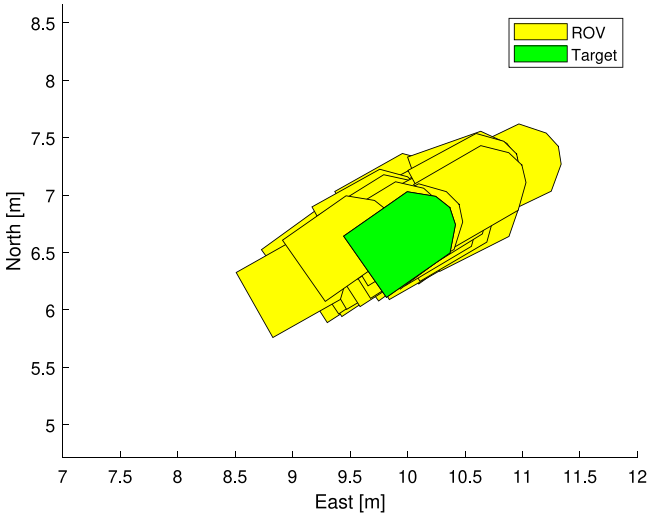

Fig. 14. DP footprint using the PD controller, field trial.

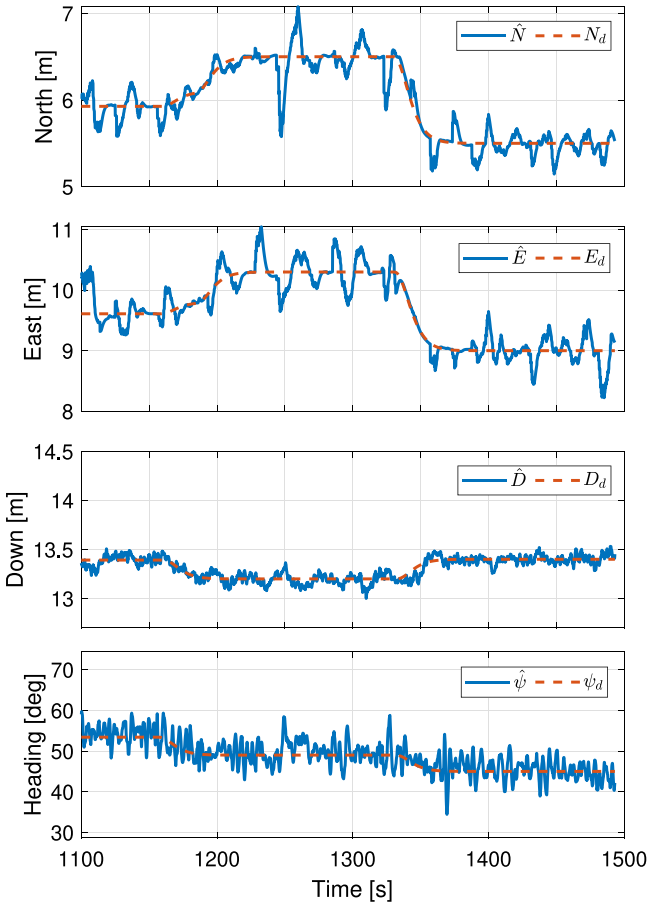

Fig. 15. Setpoint changes using the proposed controller. In descending order: North, East, Down and Heading angle. Results from field trial.

and non-linear damping, however, converged to values that could be characterized as realistic.

Fig. 20 shows a zoomed image of the desired PE reference and the estimated position in North as well as the error between them. From this result, it appears that the proposed controller also handles time-varying reference signals. The calculated and applied control forces

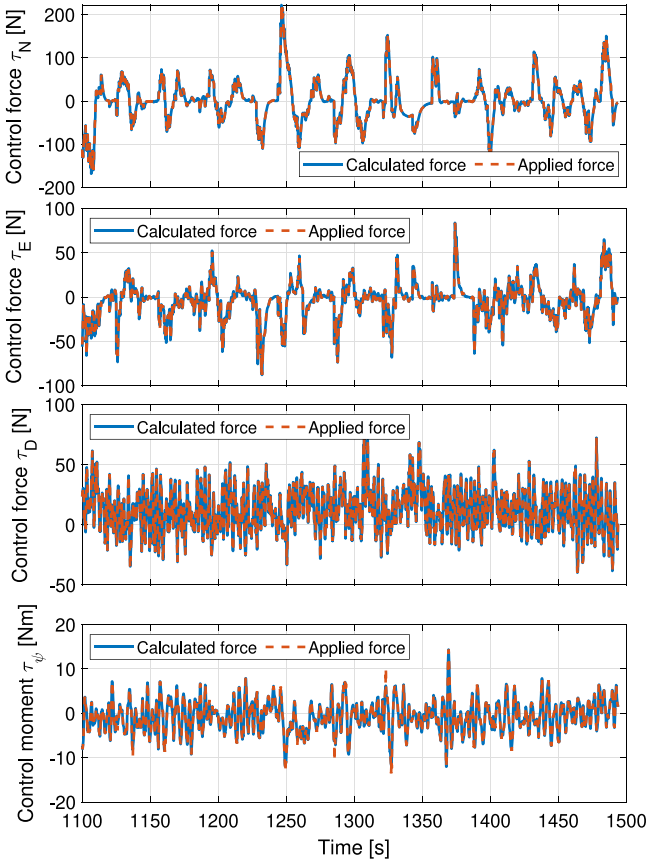

Fig. 16. The calculated and applied control forces during the position change using the proposed controller. Results from field trial.

are shown in Fig. 21. The applied control forces follows the calculated control forces for this scenario as well.

5. Conclusion

In this paper, an adaptive backstepping control law for dynamic positioning of an ROV has been presented. The controller adapts the unknown system parameters and the unknown ocean currents. Lyapunov stability theory and Matrosov's Theorem were used to prove that the origin of the closed-loop system is: (i) globally asymptotically stable when assuming persistency of excitation, and (ii) stable and bounded, with the position converging to its reference when there is no persistency of excitation.

The results of the proof were explored in simulation and experiments. The simulation examples carried out on a control plant model show that the controller is able to hold the desired position with very low deviations from the reference target, as well as move between desired positions when a new reference target is given by the operator. Furthermore, under the persistency of excitation condition, the simulations show that the estimated parameters converge to the true values and that the ROV tracks a time-varying reference signal. A comparison with two similar controllers – a controller with only disturbance adaptation and a controller with integral augmentation – was carried out and a numerical comparison of the simulation results shows that the proposed controller has a lower error norm and a lower integrated absolute error compared to these two controllers.

The proposed controller was applied to the Argus Mini ROV and validated through experiments executed in a full scale operational fish farm. The control law is able to perform the objective of holding the target position and has a low mean deviation from the target position

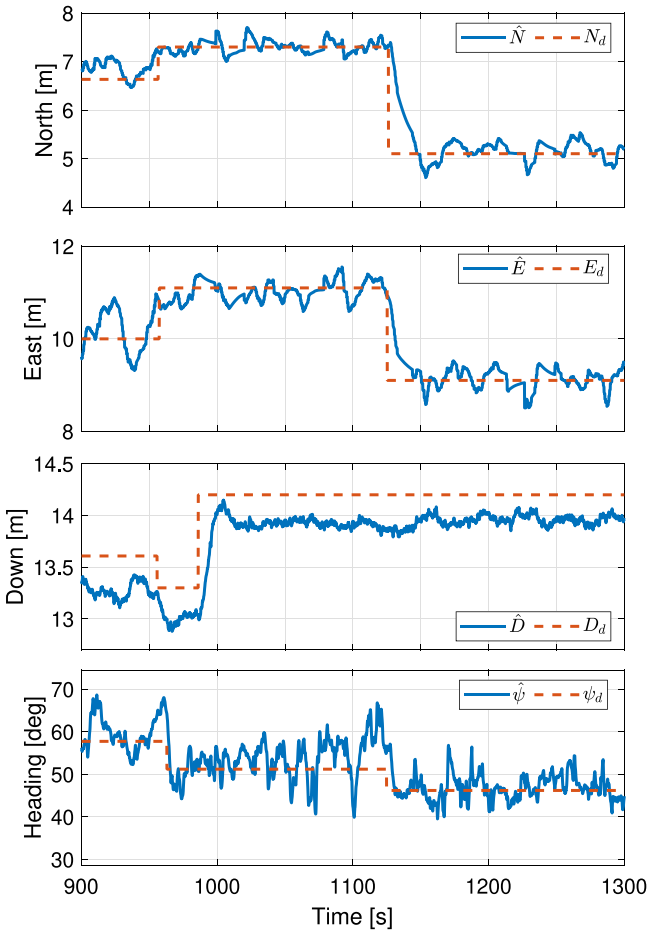

Fig. 17. Setpoint changes using the PD controller. In descending order: North, East, Down and Heading angle. Results from field trial.

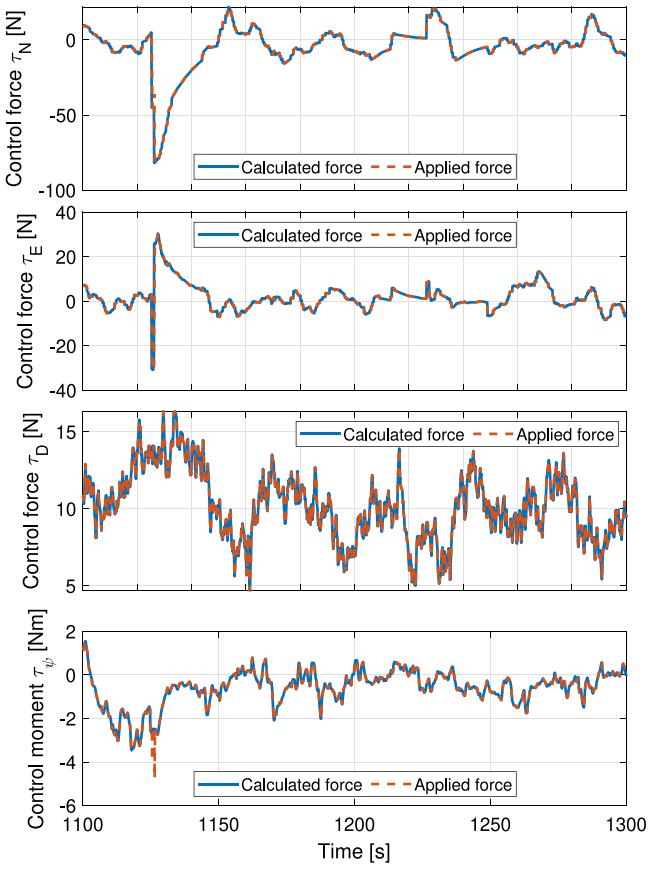

Fig. 18. The calculated and applied control forces during the position change using the PD controller. Results from field trial.

during DP. The existing PD controller implemented on the ROV had less oscillatory input signals, and its performance could perhaps be improved with a different tuning. As such, it is not concluded that the proposed controller is better or worse than the existing PD controller, rather the comparison of the two controllers is used to conclude proper and adequate functionality for the proposed controller. A persistently exciting reference signal was applied in the field trial in an attempt to estimate the ROV's parameters. The damping and current parameters tends to realistic values, but the mass parameter was incorrectly estimated. The controller was, however, able to track the varying reference signal.

As future work the authors suggest modifying the proposed control law to also include velocity control, which is often used in path following scenarios. This would require extending the control plant model to also include Coriolis and centripetal effects as these are more prominent at higher velocities. Experience gained during the field trial suggests that a projection operator should be applied to the adaptation laws to stop parameter drift and to prevent the estimated parameters from converging to non-physical values. Furthermore, the controller can benefit from a real-world comparison with similar controllers, e.g., backstepping controllers employing integral action instead of adaptation (Skjetne & Fossen, 2004).

Declaration of competing interest

The authors declare that they have no known competing financial interests or personal relationships that could have appeared to influence the work reported in this paper.

Acknowledgments

The work presented in this publication was supported by the Research based Innovation Center (SFI), Norway Exposed (RCN project number 237790) and by the SINTEF Ocean RACE, Norway internal funding program. The authors greatly appreciates the support. No conflicts of interest are declared.

Appendix A

Mass and damping matrices used in the simulation model are

$$\boldsymbol{M}_{RB} = \text{diag}\begin{bmatrix}90 & 90 & 90 & 13\end{bmatrix}$$
$$\boldsymbol{M}_{A} = \text{diag}\begin{bmatrix}54 & 72 & 360 & 5.2\end{bmatrix}$$
$$\boldsymbol{D}_{l} = \text{diag}\begin{bmatrix}250 & 200 & 175 & 15\end{bmatrix}$$
$$\boldsymbol{D}_{n} = \text{diag}\begin{bmatrix}350|u| & 350|v| & 400|w| & 75|r|\end{bmatrix}$$
$$\boldsymbol{g}(\boldsymbol{\eta}) = \begin{bmatrix}0 & 0 & 98.1 & 0\end{bmatrix}^{\mathrm{T}}.$$

Units are given in SI.

The thruster allocation has the form

$$\boldsymbol{\tau} = \boldsymbol{B}\boldsymbol{f}$$

where the thruster allocation matrix is

$$\boldsymbol{B} = \begin{bmatrix} \cos(35°) & \cos(35°) & \cos(35°) & \cos(35°) & 0 & 0 \\ \sin(35°) & -\sin(35°) & -\sin(35°) & \sin(35°) & 0 & 0 \\ 0 & 0 & 0 & 0 & 1 & 1 \\ 0 & 0 & 0 & 0 & 0 & 0 \\ 0 & 0 & 0 & 0 & 0.216 & 0.216 \\ b_1 & b_2 & b_3 & b_4 & 0 & 0 \end{bmatrix}$$

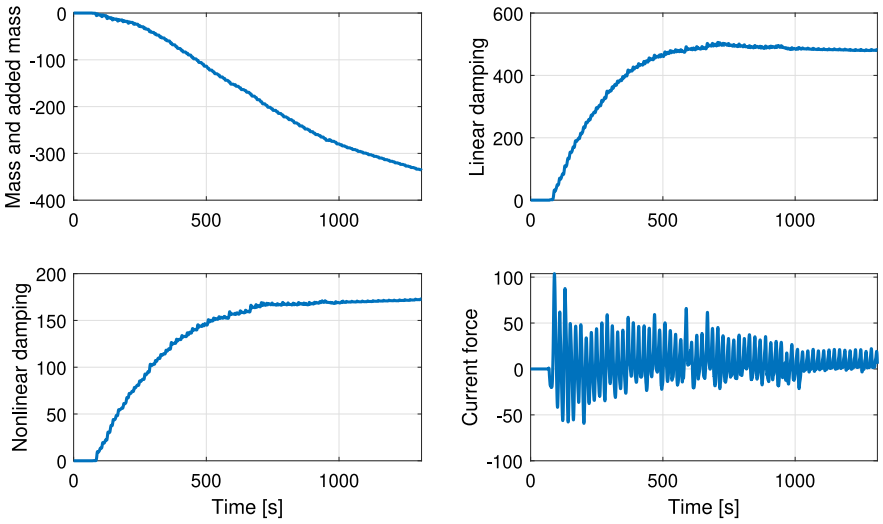

Fig. 19. The estimated parameters in the North degree of freedom, field trial.

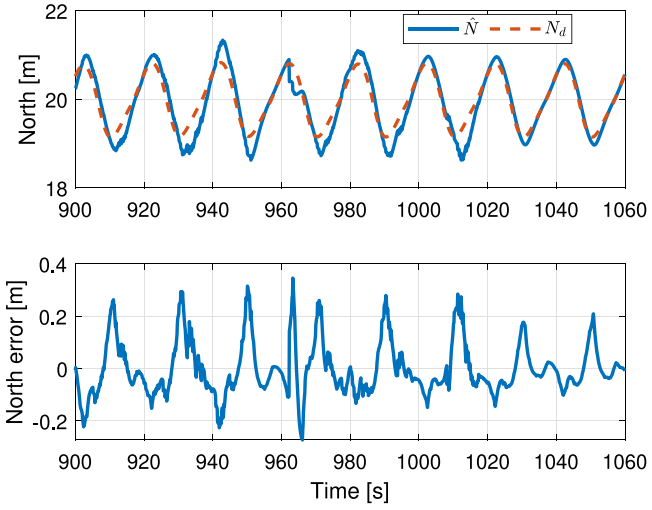

Fig. 20. The position and desired position in the North degree of freedom, and the corresponding error signal during the parameter estimation experiment. Results from field trial.

where

$$b_1 = 0.216\cos(35°) + 0.202\sin(35°),$$
$$b_2 = -0.216\cos(35°) + 0.202\sin(35°)$$
$$b_3 = 0.265\cos(35°) - 0.195\sin(35°),$$
$$b_4 = -0.265\cos(35°) - 0.195\sin(35°)$$

and the thruster vector is

$$\boldsymbol{f} = \begin{bmatrix} f_1 & f_2 & f_3 & f_4 & f_5 & f_6 \end{bmatrix}^{\mathrm{T}}.$$

The rate slew limiter is

$$y_k = \begin{cases} 1.5\left(t_k - t_{k-1}\right) + y_{k-1}, & \frac{u_k - y_{k-1}}{t_k - t_{k-1}} \geq 1.5 \\ -1.5\left(t_k - t_{k-1}\right) + y_{k-1}, & \frac{u_k - y_{k-1}}{t_k - t_{k-1}} \leq 1.5 \\ u_k, \quad \text{else} \end{cases}$$

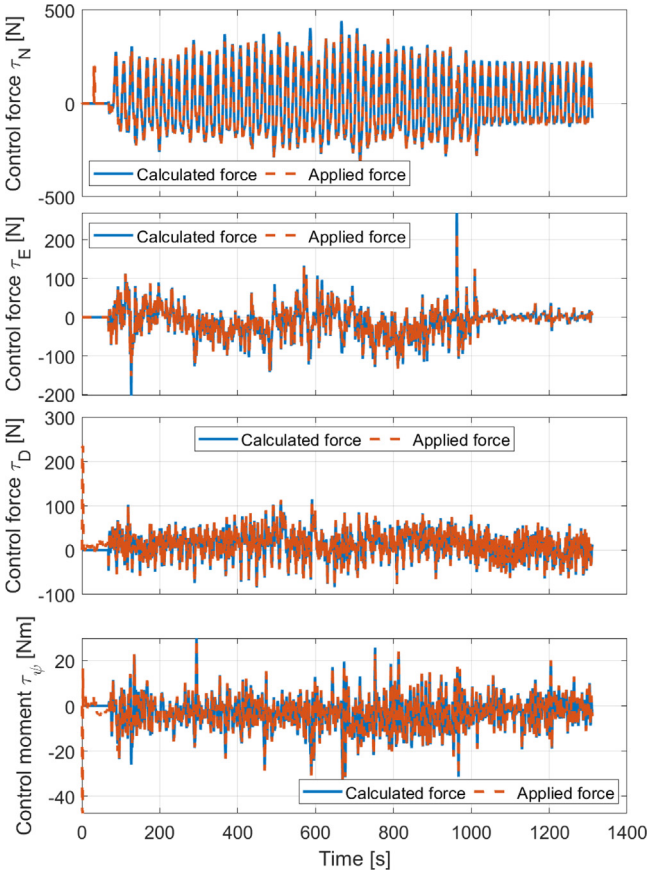

Fig. 21. The calculated and applied control forces during the trial with a persistently exciting reference signal. Results from field trial.

where t_k is the time at step k, u_k is the commanded input at step k, and y_k is the output at step k.

Appendix B

The matrix $\boldsymbol{\Phi}$ and the vector $\boldsymbol{\Psi}$ are

$$\boldsymbol{\Phi} = \begin{bmatrix} \dot{u}_v & 0 & 0 & 0 \\ 0 & \dot{v}_v & 0 & 0 \\ 0 & 0 & \dot{w}_v & 0 \\ 0 & 0 & 0 & \dot{r}_v \\ u & 0 & 0 & 0 \\ 0 & v & 0 & 0 \\ 0 & 0 & w & 0 \\ 0 & 0 & 0 & r \\ |u|u & 0 & 0 & 0 \\ 0 & |v|v & 0 & 0 \\ 0 & 0 & |w|w & 0 \\ 0 & 0 & 0 & |r|r \\ 0 & 0 & 1 & 0 \\ -\cos(\psi) & \sin(\psi) & 0 & 0 \\ -\sin(\psi) & -\cos(\psi) & 0 & 0 \end{bmatrix}, \boldsymbol{\Psi} = \begin{bmatrix} m - X_{\dot{u}} \\ m - Y_{\dot{v}} \\ m - Z_{\dot{w}} \\ I_z - N_{\dot{r}} \\ X_u \\ Y_v \\ Z_v \\ N_r \\ X_{|u|u} \\ Y_{|v|v} \\ Z_{|w|w} \\ N_{|r|r} \\ g_z \\ \tau_c^x \\ \tau_c^y \end{bmatrix}.$$

The controller parameters and adaptation gains used in the simulations are as follows:

Simulation without persistency of excitation - Section 4.1

$\boldsymbol{K}_1 = \text{diag}(5,5,5,1)$ $\boldsymbol{K}_2 = 30\boldsymbol{I}_{4\times4}$, $\boldsymbol{\Gamma} = 50\boldsymbol{I}_{15\times15}$.

Simulation with persistency of excitation - Section 4.2

$\boldsymbol{K}_1 = 0.5\boldsymbol{I}_{4\times4}$, $\boldsymbol{K}_2 = 30\boldsymbol{I}_{4\times4}$, $\boldsymbol{\Gamma} = 50\boldsymbol{I}_{15\times15}$.

Elements $[1,1]$, $[5,5]$ and $[9,9]$ of $\boldsymbol{\Gamma}$ are 1000, 1000 and 300, respectively.

Simulation with external disturbance adaptation - Section 4.3.1

$\boldsymbol{K}_1 = \text{diag}(5,5,5,1)$ $\boldsymbol{K}_2 = 30\boldsymbol{I}_{4\times4}$, $\boldsymbol{\Gamma} = 0\boldsymbol{I}_{15\times15}$.

Elements $[13,13]$, $[14,14]$ and $[15,15]$ of $\boldsymbol{\Gamma}$ are 50.

Simulation with integral augmentation - Section 4.3.2

$\boldsymbol{K}_1 = \text{diag}(5,5,5,1)$ $\boldsymbol{K}_2 = 30\boldsymbol{I}_{4\times4}$, $\boldsymbol{K}_I = \text{diag}(50,50,20,50)$.

Field trial

In the field trial, the parameters of the proposed controller are:

$\boldsymbol{K}_1 = \text{diag}\,(0.5,0.5,0.5,10)$, $\boldsymbol{K}_2 = \text{diag}\,(30,30,30,0.5)$.

The adaptation gain matrix is

$\boldsymbol{\Gamma} = 50\boldsymbol{I}_{15\times15}$,

except elements $\boldsymbol{\Gamma}[4,4] = \boldsymbol{\Gamma}[8,8] = \boldsymbol{\Gamma}[12,12] = 0.5$.

The parameters of the controller from Fossen (2011, Sec. 13.3.9) are:

$\boldsymbol{K}_p = \text{diag}\,(30,30,40,10)$, $\boldsymbol{K}_d = \text{diag}\,(0.2,0.2,0.1,0.2)$.

All units are given in SI.

References

Amundsen, H. B., Caharija, W., & Pettersen, K. Y. (2022). Autonomous ROV inspections of aquaculture net pens using DVL. *IEEE Journal of Oceanic Engineering*, *47*(1), 1–19.

Antonelli, G. (2014). *Underwater robots*. Springer.

Antonelli, G., Caccavale, F., Chiaverini, S., & Fusco, G. (2003). A novel adaptive control law for underwater vehicles. *IEEE Transactions on Control Systems Technology*, *11*(2), 221–232.

Antonelli, G., Chiaverini, S., Sarkar, N., & West, M. (2001). Adaptive control of an autonomous underwater vehicle: experimental results on ODIN. *IEEE Transactions on Control Systems Technology*, *9*(5), 756–765.

Argus Remote Systems (2021). Website. https://www.argus-rs.no/argus-rovs/11/argus-mini. (Acessed 25 October 2021).

Bannister, J., Sievers, M., Bush, F., & Bloecher, N. (2019). Biofouling in marine aquaculture: a review of recent research and developments. *Biofouling*, *35*(6), 631–648.

Bibuli, M., Caccia, M., Lapierre, L., & Bruzzone, G. (2012). Guidance of unmanned surface vehicles: Experiments in vehicle following. *IEEE Robotics & Automation Magazine*, *19*(3), 92–102.

Caharija, W., Pettersen, K. Y., Bibuli, M., Calado, P., Zereik, E., Braga, J., Gravdahl, J. T., Sørensen, A. J., Milovanović, M., & Bruzzone, G. (2016). Integral line-of-sight guidance and control of underactuated marine vehicles: Theory, simulations, and experiments. *IEEE Transactions on Control Systems Technology*, *24*(5), 1623–1642.

Candeloro, M., Sørensen, A. J., Longhi, S., & Dukan, F. (2012). Observers for dynamic positioning of ROVs with experimental results. *IFAC Proceedings Volumes*, *45*(27), 85–90, 9th IFAC Conference on Manoeuvring and Control of Marine Craft.

Capocci, R., Omerdic, E., Dooly, G., & Toal, D. (2018). Fault-tolerant control for ROVs using control reallocation and power isolation. *Journal of Marine Science and Engineering*, *6*(2), 40.

DNV GL (2015). *Dynamic positioning systems - operation guidance*: *Technical Report DNVGL-RP-E307*, DNV GL AS.

Du, J., Hu, X., Krstić, M., & Sun, Y. (2018). Dynamic positioning of ships with unknown parameters and disturbances. *Control Engineering Practice*, [ISSN: 0967-0661] *76*, 22–30.

Fernandes, D. d. A., Sørensen, A. J., Pettersen, K. Y., & Donha, D. C. (2015). Output feedback motion control system for observation class ROVs based on a high-gain state observer: Theoretical and experimental results. *Control Engineering Practice*, *39*, 90–102.

Fossen, T. I. (2011). *Handbook of marine craft hydrodynamics and motion control*. John Wiley & Sons.

Fossen, T. I., & Berge, S. P. (1997). Nonlinear vectorial backstepping design for global exponential tracking of marine vessels in the presence of actuator dynamics. In *Proceedings of the 36th IEEE Conference on decision and control, vol. 5* (pp. 4237–4242). IEEE.

Fossen, T. I., & Fjellstad, O.-E. (1995). Robust adaptive control of underwater vehicles: A comparative study. *IFAC Proceedings Volumes*, *28*(2), 66–74.

Fossen, T. I., & Grovlen, A. (1998). Nonlinear output feedback control of dynamically positioned ships using vectorial observer backstepping. *IEEE Transactions on Control Systems Technology*, *6*(1), 121–128.

Fossen, T. I., & Pettersen, K. Y. (2014). On uniform semiglobal exponential stability (USges) of proportional line-of-sight guidance laws. *Automatica*, *50*(11), 2912–2917.

Fossen, T. I., & Sagatun, S. I. (1991). Adaptive control of nonlinear underwater robotic systems. *Modeling, Identification and Control*, *12*(2), 95–105.

Hoang, N. Q., & Kreuzer, E. (2007). Adaptive PD-controller for positioning of a remotely operated vehicle close to an underwater structure: Theory and experiments. *Control Engineering Practice*, *15*(4), 411–419.

Holden, C., & Pettersen, K. Y. (2007). Robust globally exponentially stabilizing control law for fully actuated 6-DOF AUVs. *Control applications in marine systems*, *7*(1), 343–348.

Ioannou, P. A., & Sun, J. (2012). *Robust adaptive control*. Courier Dover Publications.

Jensen, Ø., Dempster, T., Thorstad, E., Uglem, I., & Fredheim, A. (2010). Escapes of fishes from norwegian sea-cage aquaculture: causes, consequences and prevention. *Aquaculture Environment Interactions*, *1*(1), 71–83.

Jónsdóttir, K. E., Klebert, P., Volent, Z., & Alfredsen, J. A. (2021). Characteristic current flow through a stocked conical sea-cage with permeable lice shielding skirt. *Ocean Engineering*, *223*, Article 108639.

Karimi, H. R., & Lu, Y. (2021). Guidance and control methodologies for marine vehicles: A survey. *Control Engineering Practice*, *111*, Article 104785.

Khalil, H. K. (2002). *Nonlinear systems, vol. 3*. Prentice Hall.

Kinsey, J. C., & Whitcomb, L. L. (2007). Model-based nonlinear observers for underwater vehicle navigation: Theory and preliminary experiments. In *Proceedings 2007 IEEE International conference on robotics and automation* (pp. 4251–4256). IEEE.

Landstad, O., Halvorsen, H. S., Øveraas, H., Smines, V., & Johansen, T. A. (2021). Dynamic positioning of ROV in the wave zone during launch and recovery from a small surface vessel. *Ocean Engineering*, *235*, Article 109382.

Lima, G. S., Trimpe, S., & Bessa, W. M. (2020). Sliding mode control with Gaussian process regression for underwater robots. *Journal of Intelligent and Robotic Systems*, *99*, 487–498.

Loria, A., Fossen, T., & Panteley, E. (2000). A separation principle for dynamic positioning of ships: theoretical and experimental results. *IEEE Transactions on Control Systems Technology*, *8*(2), 332–343.

Loría, A., Kelly, R., & Teel, A. R. (2005). Uniform parametric convergence in the adaptive control of mechanical systems. *European Journal of Control*, *11*(2), 87–100.

Makavita, C. D., Jayasinghe, S. G., Nguyen, H. D., & Ranmuthugala, D. (2017). Experimental study of command governor adaptive control for unmanned underwater vehicles. *IEEE Transactions on Control Systems Technology*, *27*(1), 332–345.

Martins, R., Dias, P. S., Marques, E. R., Pinto, J., Sousa, J. B., & Pereira, F. L. (2009). IMC: A communication protocol for networked vehicles and sensors. In *Oceans 2009-Europe* (pp. 1–6). IEEE.

Matrosov, V. (1962). On the stability of motion. *Journal of Applied Mathematics and Mechanics*, *26*(5), 1337–1353.

Moe, S., Caharija, W., Pettersen, K. Y., & Schjolberg, I. (2014). Path following of underactuated marine surface vessels in the presence of unknown ocean currents. In *American control conference (ACC), 2014* (pp. 3856–3861). IEEE.

Ohrem, S. J., Kristoffersen, T. T., & Holden, C. (2017). Adaptive feedback linearizing control of a gas liquid cylindrical cyclone. In *2017 IEEE Conference on control technology and applications* (pp. 1981–1987). IEEE.

Omerdic, E., & Roberts, G. (2004). Thruster fault diagnosis and accommodation for open-frame underwater vehicles. *Control Engineering Practice*, *12*(12), 1575–1598.

Qiao, L., & Zhang, W. (2019). Double-loop integral terminal sliding mode tracking control for UUVs with adaptive dynamic compensation of uncertainties and disturbances. *IEEE Journal of Oceanic Engineering*, *44*(1), 29–53. http://dx.doi.org/10.1109/JOE.2017.2777638.

Reite, K.-J., Føre, M., Aarsæ ther, K. G., Jensen, J., Rundtop, P., Kyllingstad, L. T., Endresen, P. C., Kristiansen, D., Johansen, V., & Fredheim, A. (2014). Fhsim—time domain simulation of marine systems. In *International conference on offshore mechanics and arctic engineering, vol. 45509*. American Society of Mechanical Engineers, V08AT06A014.

Rundtop, P., & Frank, K. (2016). Experimental evaluation of hydroacoustic instruments for ROV navigation along aquaculture net pens. *Aquacultural Engineering*, *74*, 143–156.

Skjetne, R., & Fossen, T. I. (2004). On integral control in backstepping: Analysis of different techniques. In *Proceedings of the 2004 American control conference, vol. 2* (pp. 1899–1904). IEEE.

Slotine, J.-J. E., & Li, W. (1991). *Applied nonlinear control*. Prentice Hall.

Smallwood, D. A., & Whitcomb, L. L. (2004). Model-based dynamic positioning of underwater robotic vehicles: theory and experiment. *IEEE Journal of Oceanic Engineering*, *29*(1), 169–186.

Sørensen, A. J. (2013). *Marine control systems, lecture notes*. Department of Marine Technology, NTNU.

Su, B., Reite, K.-J., Føre, M., Aarsæther, K. G., Alver, M. O., Endresen, P. C., Kristiansen, D., Haugen, J., Caharija, W., & Tsarau, A. (2019). A multipurpose framework for modelling and simulation of marine aquaculture systems. In *International conference on offshore mechanics and arctic engineering, vol. 58837*. American Society of Mechanical Engineers, V006T05A002.

Thorvaldsen, T., Holmen, I. M., & Moe, H. K. (2015). The escape of fish from Norwegian fish farms: Causes, risks and the influence of organisational aspects. *Marine Policy*, *55*, 33–38.

Vasilijević, A., Nađ, Đ., Mandić, F., Mišković, N., & Vukić, Z. (2017). Coordinated navigation of surface and underwater marine robotic vehicles for ocean sampling and environmental monitoring. *IEEE/ASME Transactions on Mechatronics*, *22*(3), 1174–1184.

Wang, Z., Liu, Y., Guan, Z., & Zhang, Y. (2021). An adaptive sliding mode motion control method of remote operated vehicle. *IEEE Access*, *9*, 22447–22454.

Yan, Z., Wang, M., & Xu, J. (2019). Robust adaptive sliding mode control of underactuated autonomous underwater vehicles with uncertain dynamics. *Ocean Engineering*, [ISSN: 0029-8018] *173*, 802–809. http://dx.doi.org/10.1016/j.oceaneng.2019.01.008, URL https://www.sciencedirect.com/science/article/pii/S0029801819300095.

Zhao, B., Blanke, M., & Skjetne, R. (2012). Particle filter ROV navigation using hydroacoustic position and speed log measurements. In *2012 American control conference* (pp. 6209–6215). IEEE.

Zhu, K., & Gu, L. (2011). A MIMO nonlinear robust controller for work-class ROVs positioning and trajectory tracking control. In *2011 Chinese control and decision conference* (pp. 2565–2570). IEEE.